Distribution and direct radiative forcing of carbonaceous and sulfate aerosols in an interactive size-resolving aerosol–climate model

Dongchul Kim,[1] Chien Wang,[1] Annica M. L. Ekman,[2] Mary C. Barth,[3] and Phil J. Rasch[3]

[1] A multimode, two-moment aerosol model has been incorporated in the NCAR CAM3 to develop an interactive aerosol–climate model and to study the impact of anthropogenic aerosols on the global climate system. Currently, seven aerosol modes, namely three for external sulfate and one each for external black carbon (BC), external organic carbon (OC), sulfate/BC mixture (MBS; with BC core coated by sulfate shell), and sulfate/OC mixture (MOS; a uniform mixture of OC and sulfate) are included in the model. Both mass and number concentrations of each aerosol mode, as well as the mass of carbonaceous species in the mixed modes, are predicted by the model so that the chemical, physical, and radiative processes of various aerosols can be formulated depending on aerosol's size, chemical composition, and mixing state. Comparisons of modeled surface and vertical aerosol concentrations, as well as the optical depth of aerosols with available observations and previous model estimates, are in general agreement. However, some discrepancies do exist, likely caused by the coarse model resolution or the constant rates of anthropogenic emissions used to test the model. Comparing to the widely used mass-only method with prescribed geometric size of particles (one-moment scheme), the use of prognostic size distributions of aerosols based on a two-moment scheme in our model leads to a significant reduction in optical depth and thus the radiative forcing at the top of the atmosphere (TOA) of particularly external sulfate aerosols. The inclusion of two types of mixed aerosols alters the mass partitioning of carbonaceous and sulfate aerosol constituents: about 35.5%, 48.5%, and 32.2% of BC, OC, and sulfate mass, respectively, are found in the mixed aerosols. This also brings in competing effects in aerosol radiative forcing including a reduction in atmospheric abundance of BC and OC due to the shorter lifetime of internal mixtures (cooling), a mass loss of external sulfate to mixtures (warming), and an enhancement in atmospheric heating per BC mass due to the stronger absorption extinction of the MBS than external BC (warming). The combined result of including a prognostic size distribution and the mixed aerosols in the model is a much smaller total negative TOA forcing (-0.12 W m^{-2}) of all carbonaceous and sulfate aerosol compounds compared to the cases using one-moment scheme either excluding or including internal mixtures (-0.42 and -0.71 W m^{-2}, respectively). In addition, the global mean all-sky TOA direct forcing of aerosols is significantly more positive than the clear-sky value due to the existence of low clouds beneath the absorbing (external BC and MBS) aerosol layer, particularly over a dark surface. An emission reduction of about 44% for BC and 38% of primary OC is found to effectively change the TOA radiative forcing of the entire aerosol family by -0.14 W m^{-2} for clear-sky and -0.29 W m^{-2} for all-sky.

[1]Department of Earth, Atmosphere and Planetary Science, Massachusetts Institute of Technology, Cambridge, Massachusetts, USA.
[2]Department of Meteorology, Stockholm University, Stockholm, Sweden.
[3]National Center for Atmospheric Research, Boulder, Colorado, USA.

1. Introduction

[2] Anthropogenic aerosol, primarily emitted or secondarily formed as the result of human activities, is a critical factor in both current and future climate [*Schwartz*, 1996, 2004; *Ramaswamy et al.*, 2001; *Forster et al.*, 2007]. However, despite substantial advances in understanding

aerosol physical and chemical processes, the uncertainty in estimating the global atmospheric abundance and radiative forcing of these aerosols remains high due to various difficulties in simulating their properties including for instance absorption and emissions in climate models [e.g., *Forster et al.*, 2007]. This is demonstrated by the significant discrepancy among previous modeling studies, and between modeled results and estimations made based on satellite data as well as ground-based measurements [*Yu et al.*, 2006; *Forster et al.*, 2007]. The mean global radiative forcing of anthropogenic aerosols at the top of the atmosphere (TOA) derived from various modeling studies as reported in the Fourth Assessment Report of the Intergovernmental Panel on Climate Change (IPCC AR4 [*Forster et al.*, 2007]) is -0.68 ± 0.24 for clear-sky and -0.22 ± 0.16 W m^{-2} for all sky. A recent model study showed an even weaker net forcing of -0.11 W m^{-2} [*Koch et al.*, 2007]. On the other hand, recent studies using satellite data estimate the annual mean direct clear-sky and all-sky radiative forcing by anthropogenic aerosols at the TOA to be -1.9 ± 0.3 and -0.8 ± 0.1 W m^{-2} as a global average [*Bellouin et al.*, 2005], or -1.4 ± 0.4 and -0.5 ± 0.33 W m^{-2} over the oceans [*Kaufman et al.*, 2005; *Yu et al.*, 2006], about a doubling of the modeled results.

[3] The uncertainties in estimating important aerosol properties can arise due to our insufficient understanding in physical and chemical properties of anthropogenic aerosols or due to simplified treatments of these processes in numerical models and data analyses. The aerosol size distribution and aerosol mixing state are two key parameters in calculating the aerosol lifecycle and its radiative effect; however, they have yet to be explicitly predicted in the majority of previous models. Traditionally, only the aerosol mass mixing ratio is predicted in global models so that number concentration and other parameters would have to be prescribed [e.g., *Kiehl and Brieleb*, 1993; *Myhre et al.*, 1998; *Koch et al.*, 1999; *Penner et al.*, 2001; *Takemura et al.*, 2005]. This so-called single moment scheme can be categorized as the simplest modal model that requires much lower computational need than a higher order modal model (i.e., the multi-moment scheme). The size-dependent nature of aerosol processes and properties is difficult to represent in a single-moment model and this could substantially affect the modeled results [e.g. *Ekman et al.*, 2004, 2006]. As an improvement to the single moment model, new methods that better represent the size-dependent nature of aerosols have been gradually adopted in the global models [*Ghan and Schwartz*, 2007]. Among them are sectional models that explicitly predict aerosol properties of given size bins and modal models that include several aerosol "modes" defined by their chemical compositions. Specifically for modal models, the general mathematical formulation of the size distribution for each aerosol mode is prescribed such that when the mass and number concentration (and in certain cases surface area or sixth moment) of a given mode are predicted, the distribution is fully defined [e.g., *Binkowski and Shankar*, 1995; *Harrington and Kreidenweis*, 1998; *Wilson et al.*, 2001; *Liu et al.*, 2005; *Stier et al.*, 2005]. It is consistent with field measurement results that aerosols generally have multiple modes in their size distribution, which can be approximated using a lognormal size distribution [e.g., *Cantrell and Whitby*, 1978; *John et al.*, 1990;

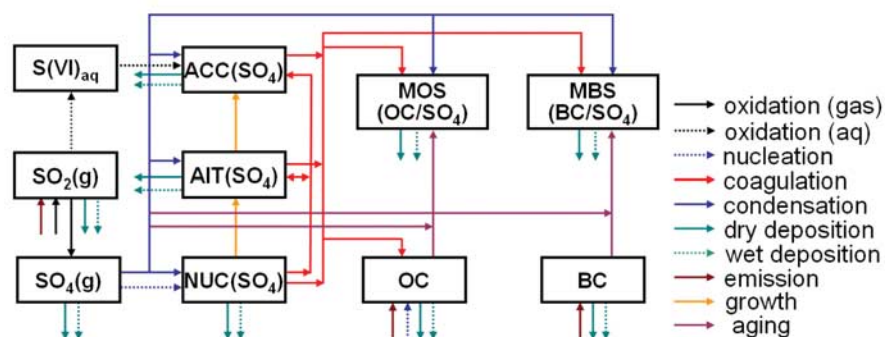*Berner et al.*, 1996; *Bond et al.*, 2004; *Clarke et al.*, 2004; *Dusek et al.*, 2004].

[4] Aerosols in the atmosphere often consist of several chemical compounds and are thus considered to be in a "mixed" state [e.g., *Ramanathan et al.*, 2001a]. The mixing state of aerosols has been evaluated by several field studies and it varies strongly with location and season [e.g., *Ramanathan et al.*, 2001b; *Hasegawa and Ohta*, 2002; *Pósfai et al.*, 2003; *Zhang et al.*, 2003; *Mallet et al.*, 2004]. Interestingly, as a special case of such mixing, a number of studies suggest that even though pure black carbon aerosols are hydrophobic they can be processed to become hydrophilic or even hygroscopic if they are coated with other chemical compounds such as sulfate or water [*Chylek and Hallett*, 1992; *Lammel and Novakov*, 1995; *Kaufman and Fraser*, 1997; *Lohmann and Leck*, 2005; *Ramanathan et al.*, 2005; *Andreae and Gelencsér*, 2006; *Mikhailov et al.*, 2006]. The radiative forcing of mixed aerosols can be significantly different than that of externally mixed ones depending on the internal structure of the mixing [e.g., *Toon and Ackerman*, 1981; *Ackerman and Toon*, 1981; *Fuller et al.*, 1999; *Jacobson*, 2000; *Andreae and Gelencsér*, 2006; *Bond et al.*, 2006]. In addition, the scavenging and thus residence time of mixed aerosols should be different than that of externally mixed aerosols. In recent years, several studies have included mixed aerosols in models [*Wilson et al.*, 2001; *Jacobson*, 2001b; *Stier et al.*, 2005; *Liu et al.*, 2005]. However, despite the importance of internal mixing in aerosol's life cycle and radiative effect, most global models still approximate aerosols as external mixtures [e.g., *Forster et al.*, 2007].

[5] We present in this paper the result of an effort to couple a multimode two-moment aerosol model of sulfate and carbonaceous species with the NCAR Community Atmospheric Model version 3 (hereafter, CAM3 [*Collins et al.*, 2006]) to investigate in particular the influences of the mixing structure as well as size distribution (2-moment vs. 1-moment or the mass-only scheme) on the distribution and the radiative impact of carbonaceous and sulfate aerosols. Note that dust and sea salt aerosols, at present are excluded from our study. These aerosols can affect directly or indirectly the anthropogenic climate effects of aerosols. For example, there is considerable impact of human activities on dust emissions [e.g., *Mahowald and Luo*, 2003] and the radiative forcing of sulfate aerosols may possibly be reduced by dust or sea salt through competing for sulfuric acid condensation [e.g., *Randles et al.*, 2004; *Bauer and Koch*, 2005]. These issues exceed the scope of this study but need to be addressed in future research. The aerosol model and its implementation to the CAM3 are described in section 2. Evaluation of the model versus various measurement data is presented in section 3, the radiative impact of aerosols is discussed in section 4. Summary and conclusions are found in section 5.

2. Model Description

2.1. Aerosol Microphysics and Chemistry Model

[6] The aerosol model was originally developed by *Wilson et al.* [2001] for simulating the global aerosol distribution. The Wilson et al. model has later been extended to include 7 aerosol modes defined by particle size

Figure 1. Schematic diagram of the physical and chemical processes included in the aerosol model. Names of aerosol mode and their chemical composition are listed in each aerosol mode. Note that wet deposition is composed of both impaction and nucleation scavenging for all modes but "NUC(SO₄)" and "BC" which includes only impaction scavenging. See the text for the detailed description.

(nucleation, Aitken, accumulation, and coarse) and hygroscopicity (4 soluble and 3 insoluble modes) and incorporated in the ECHAM5-HAM General Circulation Model [*Vignati et al.*, 2004; *Stier et al.*, 2005] and has shown to give reasonable results regarding the simulation of aerosol microphysics on a global scale. The Wilson et al. aerosol microphysics model has also been revised for cloud-resolving model applications to study aerosol-convective cloud interaction [*Ekman et al.*, 2004, 2006]. Using this aerosol model, the simulated aerosol distribution within a deep convective cloud shows good agreement with observations [A. Engström et al., personal communication, 2008].

[7] In the present study, we have further revised the model based on the version of *Ekman et al.* [2004] to incorporate it in the CAM3. The current version of the aerosol model predicts mass and number concentrations of seven aerosol modes (Figure 1 and Table 1), namely three external sulfate modes including nucleation (NUC), Aitken (AIT) and accumulation (ACC) modes; one organic carbon mode (OC); one black carbon mode (BC); one BC/sulfate mixed mode (MBS; a BC core with sulfate shell mixture, cf. section 2.1.1); and one OC/sulfate mixed mode (MOS; an internal mixture). As in *Ekman et al.* [2004], the basic coagulation and sulfuric acid condensation schemes of *Wilson et al.* [2001] are adopted in the model. Note that as in previous modeling works, BC in our model is an operational term and referred to soot aerosols containing strong sunlight-absorbing matter [e.g., *Jacobson*, 2001b; *Bond et al.*, 2004]. Certain types of aerosols with natural origin such as sea-salt and mineral dust are not included in the current experiments. More detailed descriptions of the aerosol microphysical and chemical processes that are not presented in this paper can be found in *Wilson et al.* [2001], *Ekman et al.* [2004], and *Wang* [2004].

[8] The external aerosol modes (types) in our model represent the results of commonly proposed gas-particle productions and primary emissions of aerosols. The two mixed aerosol modes are designed to reflect the potentially significant impact to aerosol radiative effects by coated BC (through altering the particle's optical properties, e.g., *Ackerman and Toon* [1981], *Bond et al.* [2006]) and mixed OC with sulfate (through reducing mass of external sulfate similar to *Bauer and Koch* [2005]), both have been ob-

served in single particle measurements [e.g., *Martins et al.*, 1998; *Pósfai et al.*, 2003; *Naoe and Okada*, 2001; *Okada et al.*, 2001; *Russell et al.*, 2002; *Okada et al.*, 2005; *Chylek et al.*, 1995]. Another consideration of including such mixtures is that both are dominated by condensation rather than the coagulation process and the former is believed to be a much faster process than the latter in mixed aerosol growth [e.g., *Riemer et al.*, 2004]. Mixtures other than the two included in our model likely exist in the real atmosphere, but these other mixtures could be approximated by external mixtures in radiation calculation via mixing rules if they mainly grow through coagulation between various aerosols and thus would not qualitatively affect our results. Note that aerosol mass partitioning results from field observations do not necessarily represent the single particle mixing state unless they were obtained by using the single particle measurement. In fact, observations have revealed that the internal mixture is not always dominant [e.g., *Pósfai et al.*, 2003; *Hara et al.*, 2003; *Schwarz et al.*, 2008] so that putting all the modeled aerosol chemical compositions into the same mixed aerosol mode might not reflect the real mixing state of aerosols in the atmosphere. Our design of the modeled aerosol structure is to include both external and internal mixtures based on commonly proposed and observed mechanisms. Our focus in this study is to explore the influence of aerosol mixing state and size distribution on radiative forcing.

[9] There are a few multi modal models that consider particle size and mixing [*Wilson et al.*, 2001; *Stier et al.*, 2005; *Liu et al.*, 2005]. However a number of differences exist between our aerosol model and these models besides their couplings to different GCMs. A key difference regard-

Table 1. Parameters for Aerosol Model[a]

Aerosol Mode	Geometric Diameter Size Interval, μm	Geometric Standard Deviation, σ	Density, g cm^{-3}
BC	–	2.0	1.0
OC	–	2.0	2.0
NUC	0–0.00584	1.59	1.8
AIT	0.00584–0.031	1.59	1.8
ACC	>0.031	1.59	1.8
MBS	–	2.0	–
MOS	–	2.0	–

[a]Density of MBS and MOS are volume ratio dependent.

ing aerosol microphysics and chemistry is that the previous aerosol models mix all modeled chemical compounds including the hydrophobic black carbon and dust in one internal mixture while our model preserves both external and internal mixtures. Specifically, our model adopts different mixing structures for different mixtures, i.e., the core-shell model for the BC-sulfate mixture and the internal mixing model for the OC-sulfate mixture, both supported by single particle measurements as indicated above. Furthermore, the representation of the aerosol microphysics presented here is based on the detailed cloud resolving modeling [*Ekman et al.*, 2004, 2006, 2007] which has been evaluated for specific case studies. The aerosol size distribution for each aerosol mode is obtained using predicted aerosol mass and number concentration and a predefined standard deviation of the lognormal distribution (σ, see Table 1). In addition, we have further modified the version of *Ekman et al.* [2004] to allow the model to predict the black carbon mass in the BC-sulfate mixture MBS (BIM) and the organic carbon mass in the MOS mode (OIM). These additional variables are used to determine the mixing states of these mixed modes and to calculate the ratio of carbonaceous species to the total mass as well as the radiative effects of these aerosols. A two-moment scheme is thus adopted utilizing the predicted mass and number concentration of aerosols in each mode at every time step for calculating the size distribution and size-dependent physical and chemical processes.

2.1.1. External Sulfate Aerosols

[10] In the model, the smallest sulfate aerosols (NUC) are produced by $H_2SO_4-H_2O$ binary nucleation [*Vehkamäki et al.*, 2002]. The primary source of gaseous H_2SO_4 is gas phase oxidation of SO_2, calculated using predicted SO_2 and DMS gaseous concentrations and a prescribed hydroxyl radical distribution adopted from *Barth et al.* [2000]. In addition, evaporation of cloud and precipitation drops also produce sulfate aerosols in the model accumulation sulfate mode by releasing aqueous sulfate to the air (see section 2.2). The aqueous production of sulfate is calculated using the CAM3 aqueous sulfate model with predicted H_2O_2 and prescribed O_3 concentrations [*Barth et al.*, 2000]. Intramode coagulations within NUC, AIT, and ACC along with intermode coagulation are included in the model to describe the evolution of each mode, providing one of the major pathways for these aerosols to grow. In addition to the coagulation process, condensation of gaseous sulfuric acid on all three sulfate modes is also included. At every time step of the aerosol model, the distribution of each sulfate mode is checked for consistency with its predefined upper bound of size and a 5% of the largest particles along with corresponding mass are moved to the adjacent mode if a violation is found [*Ekman et al.*, 2004].

2.1.2. External Carbonaceous Aerosols

[11] BC is assumed to be emitted from the surface (see section 2.3). For simplicity, no segregation of biomass burning and fossil fuel BC emissions is applied. For the organic aerosols, we include primary organic aerosols (POA) directly emitted from the surface and secondary organic aerosols (SOA) converted from biogenic VOCs (isoprene and monoterpene) using the yield coefficient suggested by *Griffin et al.* [1999]. In the current model, intramode coagulation is included for both external BC and external OC. However, intermode coagulation with sulfate is included for external OC but not for external BC under an assumption that the dominant mechanism converting the hydrophobic external BC to hygroscopic MBS is condensation of sulfuric acid on the surface of external BC.

2.1.3. Mixed Aerosols

[12] Two mixed modes are included in the current model, i.e., a BC-sulfate mixture (MBS) and OC-sulfate mixture (MOS). The former mode has a structure of BC as a core and sulfate as a shell. The latter mode has a uniformly mixed structure. The initial source of the two mixed aerosol modes is correspondingly external BC and OC. Pure BC aerosols do not absorb water (hydrophobic) but can be coated by hydrophilic substances in the atmosphere. This condensation is considered as an "aging" process in the model where the aged black carbon aerosols are introduced to the MBS as seeds. The same aging process is applied to external OC and MOS. The key transition of these particles from external to internal mixtures with sulfate in our model is the change of their hygroscopicity described by the κ value [*Petters and Kreidenweis*, 2007] used in the nucleation scavenging calculations (see section 2.3). External BC is assumed to be hydrophobic and external OC has a very low κ value. When converted to MBS or MOS, the corresponding κ value becomes either the same as (MBS) or very close to (weighted by OC and sulfate ratio in MOS) that of sulfate.

[13] In the initial aging of carbonaceous aerosols we assume that the condensation of sulfuric acid plays a dominant role [e.g., *Riemer et al.*, 2004]. The aging process of carbonaceous aerosols in the real atmosphere is not well known [e.g., *Cooke and Wilson*, 1996]. Estimated aging times (where some are based on observations) range from 0.7 to 4 days [*Wilson et al.*, 2001; *Chin et al.*, 2002; *Cooke et al.*, 2002; *Riemer et al.*, 2004; *Kanakidou et al.*, 2005]. In this study, we adopt a constant BC and OC aging time of 40 and 20 hours, respectively, based on previous studies [*Wilson et al.*, 2001; *Kanakidou et al.*, 2005]. These numbers agree well with the values derived for polluted environment by *Riemer et al.* [2004]. In reality, the aging of aerosols needs sufficient supply of sulfuric acid gas to process. Therefore in addition to the aging timescale, we also adopt an assumed shell to core radius ratio of 1.25 (which translates to a sulfate to BC mass ratio of 1.63) of aged BC in the model. Recent aircraft measurements suggest a mean core-shell mass ratio of 1.5 in the layer between surface and 15 km, and likely less than 1.5 in the lower troposphere (<5 km) [*Schwarz et al.*, 2008]. For simplicity, the same sulfuric acid mass consumed by BC aging is provided for the OC aging calculation whenever external OC exists. The total requested sulfate mass for external BC and OC aging calculated based on the aging times is then to compare with the available gaseous sulfuric acid quantity. When the total requested sulfate mass exceeds the available amount of sulfuric acid gas, the actual consumed sulfate mass along with the actual number of aged particles will be accordingly reduced. Therefore our aging scheme is confined by both aging time and availability of gaseous sulfuric acid and this is different than other schemes that only use aging time [e.g., *Wilson et al.*, 2001]. Sensitivity tests with different aging times of 20 hours and 80 hours result in differences in atmospheric burdens of BC and MBS less than 5% and 9%, respectively,

from the results derived using the reference aging time of 40 hours. This low sensitivity is likely a result of the gaseous sulfate constraint applied in the scheme.

[14] The growth of mixed aerosols in the model occurs through intramode coagulation and intermode coagulation between the mixed aerosols and the three external sulfate modes. Additionally, condensation of sulfuric acid increases the sulfate mass concentration in the mixed modes and this is a different process in the model than the aforementioned aging of external carbonaceous aerosols.

[15] The mass of black carbon in the MBS and the total mass of this mode are both prognostic variables so that the mass conservation of both quantities undergoing advection and various chemical and physical conversions are obeyed. The ratio of black carbon to total MBS mass (R_{BM}) is derived based on the above two mass quantities and thus is a time-varying diagnostic constituent. Because R_{BM} is generally rather small through the atmospheric layers, the MBS is treated as a hygroscopic aerosol. The derivation of the ratio of OC to total MOS mass, R_{OM}, follows the same method of R_{BM}. However, a homogeneous mixing structure of MOS is assumed whenever the mixing state is needed for calculation (radiation and scavenging) based on the fact that the hygroscopicity of OC aerosols makes them easy to mix with sulfate rather than forming a core-shell structure.

2.2. Dry Deposition and Cloud-Related Sinks and Sources of Aerosols

[16] Sedimentation and dry deposition of aerosols are included in the model. A constant sedimentation velocity of 0.1 cm s^{-1} with a pressure correction [*Wang*, 2004] is applied to all aerosols at all grid points. The dry deposition velocity calculation is adopted from *Wang* [2004] and is applied to all aerosol modes at the lowermost model layer, which is about 60 m above the surface. In addition, two types of cloud-related scavenging processes, i.e., impaction and nucleation scavenging, are included in the model. Impaction scavenging is the removal process of aerosols through the collection of aerosols by falling precipitating droplets in either liquid or ice phase. Since the efficiency of impaction scavenging depends on the size of the aerosol [*Seinfeld and Pandis*, 1998], each mode has a different impaction scavenging rate with the efficiency factor of 30 (NUC), 6 (AIT), 3.5 (BC, OC, MBS, and MOS), and 1.0 (ACC) based on *Ekman et al.* [2004]. The efficiency of impaction scavenging by ice particles is assumed to be half of that by liquid drops [*Wang*, 2004]. This process utilizes both convective and stratiform precipitation calculations from the physics module of CAM3.

[17] Hygroscopic aerosols can serve as cloud condensation nuclei (CCN) when an air parcel reaches supersaturation. This process leads to a loss of aerosols and is referred to as nucleation scavenging. This removal process is applied to all modes containing large hygroscopic aerosols, which potentially could be removed by nucleation scavenging i.e., OC, AIT, ACC, MBS and MOS. The size of activated aerosols is governed by the supersaturation at cloud base [*Pruppacher and Klett*, 1997; *Ekman et al.*, 2004]. To calculate aerosol activation size, the κ-Köhler theory [*Petters and Kreidenweis*, 2007] is adopted and nucleation scavenging is calculated in the grid points between 500–2000 m in altitude above ground corresponding to the

typical elevations of cloud base where this process primarily occurs [*Pruppacher and Klett*, 1997; *Wang*, 2005]. To simplify the calculations, and similar to *Adams and Seinfeld* [2002], a constant supersaturation ratio of 0.1% for OC and 0.2% for more soluble sulfate and mixed aerosols at cloud base is used. Note that parameterizations derived for general circulation models that allow the supersaturation value to vary along the upward path of an air parcel [*Abdul-Razzak et al.*, 1998; *Abdul-Razzak and Ghan*, 2000; *Nenes and Seinfeld*, 2003] are expected to improve the current nucleation scavenging scheme. The aerosol mass loss through nucleation scavenging at a given grid, C_{aer}, is calculated by summing the fraction of aerosols larger than the activation size based on the size distribution in the cloudy area of the model:

$$C_{aer} = \frac{1}{2} C_{aer}^0 \left[1 - erf \left(\frac{\log(r_c) - \log(r_m)}{2p_3} \right) \right] \times f_{cld} \qquad (1)$$

where C_{aer}^0 is the aerosol concentration before nucleation scavenging (g cm^{-3} for mass or cm^{-3} for number), r_c is the minimum activation radius of aerosols for given supersaturation ratio, r_m is the number or volume median radius of the size distribution, and p_3 is equal to ln(σ). f_{cld} is cloud fraction.

[18] When cloud droplets evaporate, aqueous sulfate inside these droplets will be released to the air and thus join the aerosol family. We assume that all aqueous sulfate mass released from this process will be added to the mass of ACC. This is consistent with previous studies [e.g., *Hoppel et al.*, 1994; *Jensen et al.*, 1996; *Feingold and Kreidenweis*, 2000; also *Pruppacher and Klett*, 1997]. The number of drops evaporated (and therefore ACC formed) is assumed to be 20 per cm^3 for cloud water droplet and 10^{-3} per cm^3 for raindrop, approximating typical cloud conditions [*Pruppacher and Klett*, 1997; *Wang*, 2005]. The conversions for mass and number are calculated as:

$$dM_{evap}\left(kg \; kg_{air}^{-1}\right) = [SO4]_{aq}\left(kg \; kg_{air}^{-1}\right) \times f_{M\_evap} \qquad (2a)$$

$$dN_{evap}\left(kg_{air}^{-1}\right) = \frac{2 \times 10^7 \times f_{C\_evap}(m^{-3}) + 10^3 \times f_{R\_evap}(m^{-3})}{\rho(kg_{air} \; m^{-3})} \times f_{cld} \qquad (2b)$$

where f_{M_evap} is the aerosol mass evaporation efficiency defined as the ratio of evaporation to total cloud water and precipitation water at each model grid and derived using CAM3 diagnostic variables. f_{C_evap} is the cloud droplet evaporation ratio defined as the ratio of cloud droplet to the total condensed water. The rain evaporation ratio of f_{R_evap} is the rain evaporation ratio to the total precipitation.

2.3. Emissions

[19] Emissions of BC and primary OC are prepared from a 1 × 1 degree emission inventory for the year of 1990 derived using the MIT Emission Prediction and Policy Analysis Model (EPPA; *Mayer et al.*, 2000; *Babiker et al.*, 2001; *Wang*, 2004). Because estimates of global aerosol emissions are still uncertain, a second inventory derived by *Bond et al.* [2004; from here Bond] is also used in certain simulations. The comparison between model results derived using these two different emissions inventories will be

discussed in section 4.3. Figure 2 shows the annual emissions of these species. The annual BC emissions of EPPA (Bond) data set are 14.4 (8.0) and the primary OC emissions are 54.4 (33.8) Tg. Both emission inventories used in this study are within the ranges of previous studies, i.e., 6.6–14 Tg year^{-1} for black carbon and 32.5–81 Tg year^{-1} for primary organic carbon aerosols. Biogenic VOC emissions of isoprene and monoterpenes of 501.7 and 127.2 TgC year^{-1}, respectively, provided by the Global Emissions Inventory Activity (GEIA, http://www.geiacenter.org/) are included for the secondary organic carbon calculations. The estimated annual SOA emission is 30.7 TgC year^{-1}. Anthropogenic SO_2 emissions from EPPA prediction of 71.4 TgS year^{-1} have been used. Assumed geometric mean radii of 10, 20, 20, and 50 nm are used in the lognormal size distributions of BC, OC, SOA, and sulfate, respectively, to derive the number concentrations of these aerosols from their emissions. The sigma value is the same as listed in Table 1. Besides SO_2 emissions, the model also includes emissions of dimethylsulfide (DMS) provided by CAM3 (based on *Kettle et al.* [1999]; 19.3 TgS year^{-1}).

[20] BC, primary OC, and DMS emissions are added to the lowest model layer and SO_2 and biogenic VOC emissions are added to the 2 lowermost model layers at every 30 minutes. Emissions of BC, primary OC, and SO_2 are constant through the entire model year. Emissions of DMS and biogenic VOCs vary monthly. The actual emission rates at each model grid are thus scaled accordingly from either annual or monthly emissions to fit into the model time step. Since our primary goal in the present study is to explore the roles of mixing states and size distributions in determining the distribution and radiative forcing of aerosols, the above simplifications in emissions should not affect our conclusion.

2.4. Radiative Effect of Aerosols

[21] The model-predicted size distributions of each aerosol mode are used in the CAM3 model to calculate the radiative effect of aerosols on solar radiation. The delta-Eddington radiation transfer model in CAM3 requires three key input aerosol optical parameters [*Briegleb*, 1992], i.e., the specific extinction coefficient (k), single scattering albedo (ω), and asymmetry parameter (g). In our model, the aerosol specific extinction, single scattering albedo, and asymmetry parameter for each aerosol are calculated using the size integration based on *Kiehl and Briegleb* [1993] and *Kiehl et al.* [2000]:

$$k(\lambda) = \frac{3}{4\rho_s} \frac{\int Q_{ext}(\lambda, r) r^2 n(r) dr}{\chi \int r^3 n(r) dr} \tag{3a}$$

$$\omega(\lambda) = \frac{\int Q_{sca}(\lambda, r) r^2 n(r) dr}{\int Q_{ext}(\lambda, r) r^2 n(r) dr} \tag{3b}$$

$$g(\lambda) = \frac{\int Q_{sca}(\lambda, r) Q_{gsa}(\lambda, r) r^2 n(r) dr}{\int Q_{sca}(\lambda, r) r^2 n](r) dr} \tag{3c}$$

where r is the aerosol particle radius, $n(r)$ is the size distribution function, ρ_s is the density of the aerosol, and χ

is the fraction of fine particle mass that is sulfate ($\chi = 0.6$ is adopted following *Kiehl and Briegleb*, 1993). The terms, $Q_{ext}(\lambda, r)$, $Q_{sca}(\lambda, r)$, and $Q_{gsa}(\lambda, r)$, are the Mie extinction efficiency, scattering efficiency, and asymmetry parameter, respectively, all derived using the code of *Bohren and Huffman* [1983; BHMIE]. The real (imaginary) refractive indices for pure BC, OC, and sulfate at 550 nm wavelength are 1.96 (−0.66), 1.53 (−0.0055), and 1.431 (−0.005), respectively, taken from *World Climate Program* [1986], *Koepke et al.* [1997], and *Palmer and Williams* [1975].

[22] Assuming that an aerosol size distribution follows a lognormal distribution, the aerosol size distribution function, $n(r)$, is expressed as [*d'Almeida et al.*, 1991]:

$$n(r) = \frac{N_{aer}}{\sqrt{2\pi} r p_3} \exp\left[-\frac{(\ln r - \ln r_m)^2}{2p_3^2}\right] \tag{4}$$
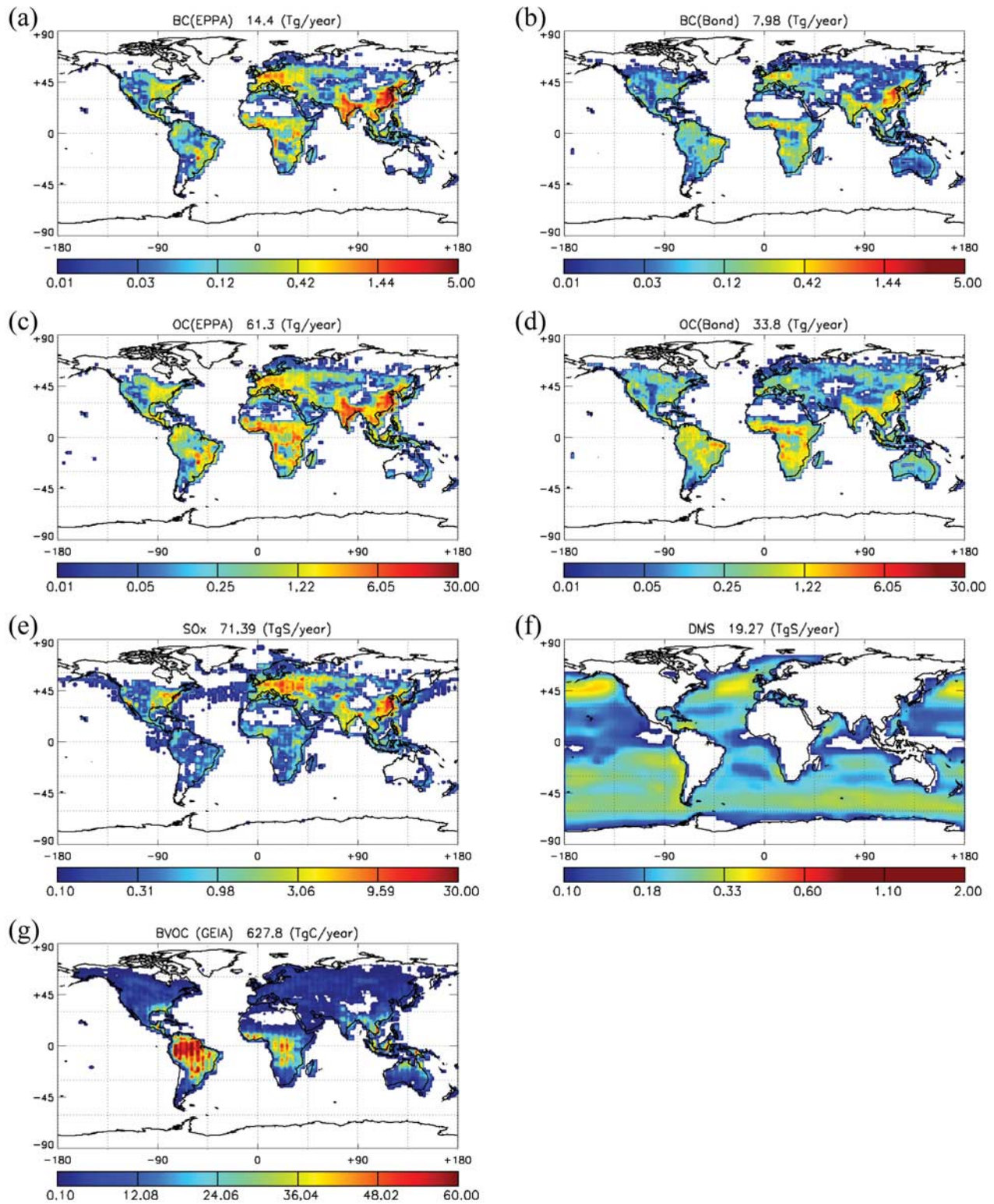
and the geometric mean radius r_m (μm) for each aerosol mode can hence be derived:

$$r_m = \left(\frac{3}{4} \frac{10^{12} M_{aer}}{\rho_{air} \pi N_{aer}} \exp\left[-4.5 p_3^2\right]\right)^{\frac{1}{3}} \tag{5}$$

where, M_{aer} (g cm^{-3}) and N_{aer} (cm^{-3}) are mass and number concentration of aerosols in a given aerosol mode and $p_3 = \ln(\sigma)$. A unit conversion factor, 10^{12} is applied in equation (5) to convert volume from cm^3 to μm^3. Using equations (4) and (5), a size-dependent calculation of aerosol radiative effect based on the two-moment scheme in the aerosol model can be implemented.

[23] Hygroscopic aerosols are known to grow following the increase of relative humidity of the surrounding air. The effect of such a growth on the aerosol optical properties has been parameterized in several studies [*Kiehl and Briegleb*, 1993; *Hess et al.*, 1998; *Kiehl et al.*, 2000]. In our model, calculated dependencies of k, ω, and g on relative humidity for the external sulfate modes are very close to those in *Kiehl and Briegleb* [1993] except for the case of k in the near IR range due to the difference in refractive indices. For soluble aerosol modes other than external sulfate, a size growth parameterization [see equation (1) in *Kiehl et al.*, 2000] as a function of relative humidity is also applied.

[24] In order to speed up the computation, k, ω, and g for all aerosol modes are tabulated with both predicted geometric mean size of the given aerosol mode and the solar wave band as indices. These tables are derived using BHMIE program based on 1000 particle size bin integrations (from 0.001 to 5.0 μm with 0.005 μm interval) for 19 wave bands in the CAM3 standard radiation module. Besides the size and hygroscopic factors, we have also included the chemical composition related mixing states in our model to calculate the radiative effects of mixed aerosols. This leads to additional dimensions in tabulating the optical properties of the mixed aerosol modes compared to the case of external ones. Specifically, the well-mixed internal mixture mode (for example OC-sulfate mixed mode in our model) requires additional dimensions of refractive indices (*Re* and *Im*). The refractive indices are obtained using volume weighted averaging over all aerosol constituents. The resultant tabulation of aerosol optical properties of well-mixed inter-

Figure 2. Distributions of BC, primary OC, SO_2, DMS, and BVOC emissions. DMS and biogenic VOCs (BVOC) are annual means from monthly data set. Color tables are in mg m^{-2} day^{-1} for BC, OC, and BVOC and in mg S m^{-2} day^{-1} for SO_2 and DMS. Two different emission data (EPPA and Bond) are presented for BC and OC. Note that different color tables are used.
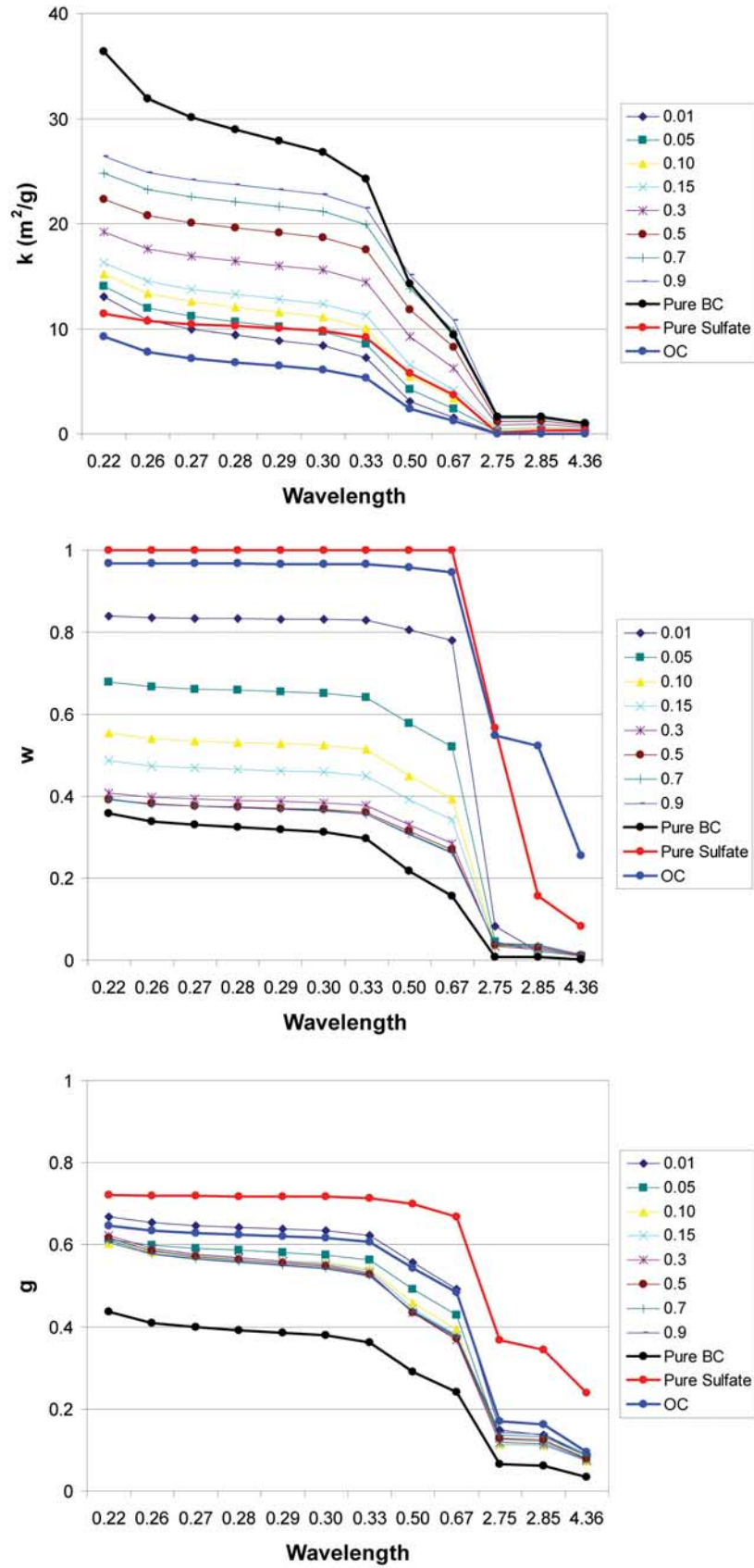
Figure 3

nal mixture is thus a function of four indices of λ, r_m, Re, and Im. A similar method has been used in other studies [*Stier et al.*, 2005, 2006, 2007].

[25] The core-shell mixing model is developed specifically for the BC/sulfate mixed aerosols (MBS) in our model with a core of BC coated by sulfate shell. The optical property tables require an additional dimension of shell-to-core radius ratio of R_{mix} besides the size and wavelength. This parameter can be derived using the model predicted BC mass ratio in the core-shell mixture, R_{BM}:

$$R_{21\,dry} = \left[1 + \frac{(1 - R_{BM\,dry})}{R_{BM\,dry}} \frac{\rho_1}{\rho_2} \right]^{1/3} \quad (6a)$$

where the indices 1 and 2 represent the core and shell, ρ_1 and ρ_2 are densities of core and shell, respectively, and the label "dry" means the dry aerosol property. The shell-to-core mass ratio of dry MBS ($R_{BM\,dry}$) is affected by the hygroscopic growth of shell (sulfate) and this effect is accounted for in equation (6b) to get the final shell-core ratio of R_{mix} (equation (6c)):

$$R_{BM\,wet} = R_{BM\,dry} \frac{1}{1 + R_{21dry}^3 (g^3 - 1) \frac{\rho_w}{\rho_1} R_{BM\,dry}} \quad (6b)$$

$$R_{21\,wet} = R_{mix} = \left[1 + \frac{(1 - R_{BM\,wet})}{R_{BM\,wet}} \frac{\rho_1}{\rho_2} \right]^{1/3} \quad (6c)$$

where ρ_1 and ρ_w are density of core and water, R_{21dry} is shell-to-core radius ratio of dry particle, and g is the growth factor of particle size and parameterized as *Kiehl et al.* [2000].

[26] Based on the given chemical compounds of the core (BC) and shell (sulfate), $R_{21\,wet}$ has values of 3.82, 2.26, 1.81, 1.61, 1.32, 1.16, 1.07, and 1.02 for given $R_{BM\,wet}$ values of 1, 5, 10, 15, 30, 50, 70, and 90 %, respectively. The optical properties of MBS are then tabulated for the above shell-core radius ratios as well as sizes and wavelengths using the Coated_Sphere program [reorganized by W. J. Wiscombe, personal communication (2005) based on *Toon and Ackerman* [1981]]. The properties are linearly interpreted using adjacent values for cases when the shell-core ratio falls between two given R_{21wet} values. Optical properties of MBS calculated using described methods are between sulfate and black carbon and are very sensitive to the mixing state of MBS (Figure 3). The most significant transition in the single scattering albedo occurs when the black carbon mass is lower than 30% of the total mass of mixed aerosol. In this low R_{BM} regime, MBS aerosol has an intermediate absorption and scattering compared to black carbon and sulfate. *Chylek et al.* [1995] showed that inclusion of a tiny amount of black carbon in sulfate can significantly change the specific absorption and single

scattering albedo. Note that the shell-core ratio used in *Chylek et al.* [1995] is greater than 10 or, in other words, BC accounts for less than 0.1% of the total aerosol mass. *Ackerman and Toon* [1981] suggested that 20% of black carbon in mixed aerosols is necessary to achieve observed values of single scattering albedo in polluted areas. The predicted R_{BM} value by our model is mostly below 35% which emphasizes the importance of an explicit treatment of mixed aerosols in the radiation calculations of the model. Note that the derived optical properties calculated based on typical modeled properties of MBS mixed aerosol in this study are very consistent with those derived in other similar studies [e.g., *Ackerman and Toon*, 1981; *Bond et al.*, 2006].

[27] Several studies have calculated the optical properties of the mixtures of BC and reflecting aerosol such as sulfate based on the well-mixed model (the same one we used to calculate MOS in our model), i.e., using the volume averaged refractive indices over all aerosol constituents. Thus it is important to contrast the core-shell mixing model with the uniformly internal mixing model [e.g., *Jacobson*, 2001a; *Chung and Seinfeld*, 2002; *Stier et al.*, 2005, 2006]. The latter method is relatively simple and fast, however, does not represent a physically valid structure for the mixture of BC and hygroscopic matters [e.g., *Martins et al.*, 1998; *Pósfai et al.*, 2003; *Naoe and Okada*, 2001] and only provides an upper limit of radiative forcing compared with the lower limit provided by external mixing assumption [e.g., *Jacobson*, 2001b]. We have tested both the well-mixed and the external mixture model in addition to the core-shell model for the MBS mixed mode and the comparison of these results is discussed in section 4.

2.5. Coupling the Aerosol Model With CAM3 and the Model Setup

[28] The aerosol model is coupled interactively with CAM3. The interface has been developed to dynamically provide CAM3-predicted wind, temperature, relative humidity, cloud fraction, and condensed water content to the aerosol model. The aerosol mass, number concentration and derived size distribution are used in turn by CAM3 in its radiation module to calculate radiative fluxes. The aerosol model calculations are done with the same time step (30 min) as the advection and physics in CAM3.

[29] The model uses a 26-layer hybrid vertical coordinate; that is, sigma coordinate near the surface while in the upper atmosphere following air pressure surfaces. The horizontal resolution is 2.5 degree in the longitudinal and 2 degree in latitudinal direction. The finite volume dynamic core is used. An observed 20-year monthly mean sea surface temperature (SST) data set is used to drive the integration.

[30] In order to test the performance of our aerosol model in comparison with the traditional one-moment scheme, we have allowed the CAM3 sulfate aerosol and chemistry model [*Barth et al.*, 2000; hereafter CAM3S] to coexist with our new aerosol model in all the simulations without interrupting each other. Both models use the same emissions

---

Figure 3. Optical properties of pure aerosols and BC-sulfate core-shell mixed aerosols as a function of wavelength (μm). Geometric mean radii of pure aerosols are 0.01, 0.02, and 0.05 (μm) for BC, OC, and sulfate, respectively. The geometric mean radii of mixed aerosols are 0.02 (μm). Optical properties of mixed aerosols with eight different R_{BM} values are shown. (a) Specific extinction. (b) Single scattering albedo. (c) Asymmetry parameter.

Table 2. Experiment Setup[a]

| Case | BC/OC Emissions | Mixing Assumptions | | Emission Type | r_g, nm BC/OC/SO$_4$ |
		MBS	MOS		
EEA	EPPA	external	external	all (BC/OC/SO$_2$)	11.8/20/50
ECA	EPPA	core-shell	homogeneous	all	varies
EHA	EPPA	homogeneous	homogeneous	all	varies
EEE	EPPA	none	none	all	11.8/20/50
ECE	EPPA	none	none	all	varies
BCA	Bond	core-shell	homogeneous	all	varies

[a]All microphysics calculations are done in two-moment methods. Note that there is no mixed aerosol in the EEE and ECE cases.

of sulfur compounds and are driven by the same amount of sulfate produced in gaseous and aqueous phase. The model procedures have been carefully designed to let them produce independent predictions.

[31] To focus on the aerosol cycle and its direct effect on radiative forcing, the model results presented below do not include the feedback of the aerosols on the radiation. Instead their effect is calculated via a diagnostic procedure. Following this procedure the clear-sky and all-sky radiative fluxes resulting from the inclusion of various aerosol modes are calculated one by one in the CAM3 radiative module and then compared with the reference clear-sky and all-sky fluxes calculated by excluding these aerosols to derive the radiative forcing of each of these modes. These diagnostic fluxes are not actually used to update the fluxes needed by the CAM3 model so that they do not perturb the climate dynamics features. Also, only solar radiative forcings are calculated for the aerosols. Six sets of model runs are performed to predict the atmospheric cycle and radiative forcing of various types of modeled aerosols and to test the sensitivity of the results to certain model processes as well as emissions data (Table 2). Each simulation lasts 5 years. The first two years of the simulations are regarded as the model spin-up period and the average of the last three years of simulation are used in the analysis unless otherwise indicated.

[32] In the EEA run, we calculate the radiative forcings of aerosols using the traditional external mixing and single moment model with predicted mass concentrations of various aerosol constituents. The total mass of black carbon in a grid cell is diagnostically derived as the sum of external BC and BC mass in MBS:

$$[BC_{total}]_i = [BC_{external}]_i + R_{BM\,i}[MBS]_i \qquad (7a)$$

The total mass of OC is calculated as:

$$[OC_{total}]_i = [OC_{external}]_i + R_{OM\,i}[MOS]_i \qquad (7b)$$

The total sulfate aerosol mass concentration is derived by:

$$[Sulfate]_i = [NUC]_i + [AIT]_i + [ACC]_i + (1 - R_{BM\,i}) \times [MBS]_i$$
$$+ \; (1 - R_{OM\,i}) \times [MOS]_i \qquad (7c)$$

Here brackets represent the mass concentrations in various aerosol modes, and R_{BM} is the BC mass ratio in MBS and R_{OM} the OC mass ratio in MOS. The diagnostic radiation calculations that mimic the externally mixed and single moment aerosol model by assuming a constant geometric mean radius for each given aerosol constituents; that is, 11.8 nm for BC, 50 nm for sulfate, and 20 nm for OC are

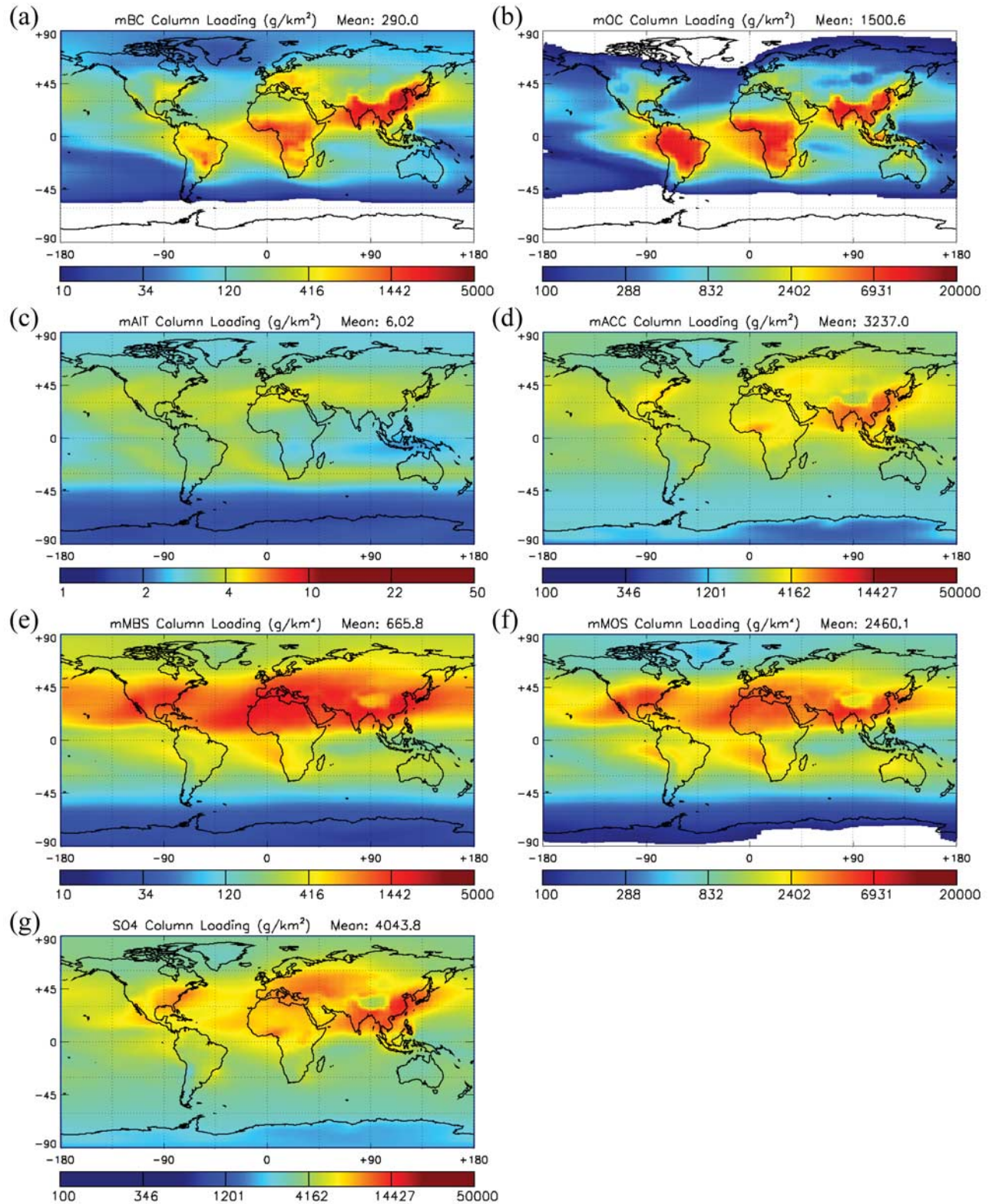processed using the mass only lookup tables to calculate the radiative forcings.

[33] The core-shell method is used to calculate the radiative forcing in the ECA and BCA runs. The ECA run uses the EPPA emissions inventory for BC and primary OC, while the BCA run uses the Bond emissions inventory. The uniformly mixed (i.e. internally mixed aerosols) radiative forcing model (using volume weighted refractive indices) is used for the EHA run. Mixing between seen different aerosol constituents is prohibited in the ECE run and therefore there are no mixed mode aerosols (i.e., MBS and MOS). Our purpose of carrying out three different radiative forcing calculations is to explore the influences of various aerosol models on the direct radiative forcing of aerosols rather than to provide a best estimate.
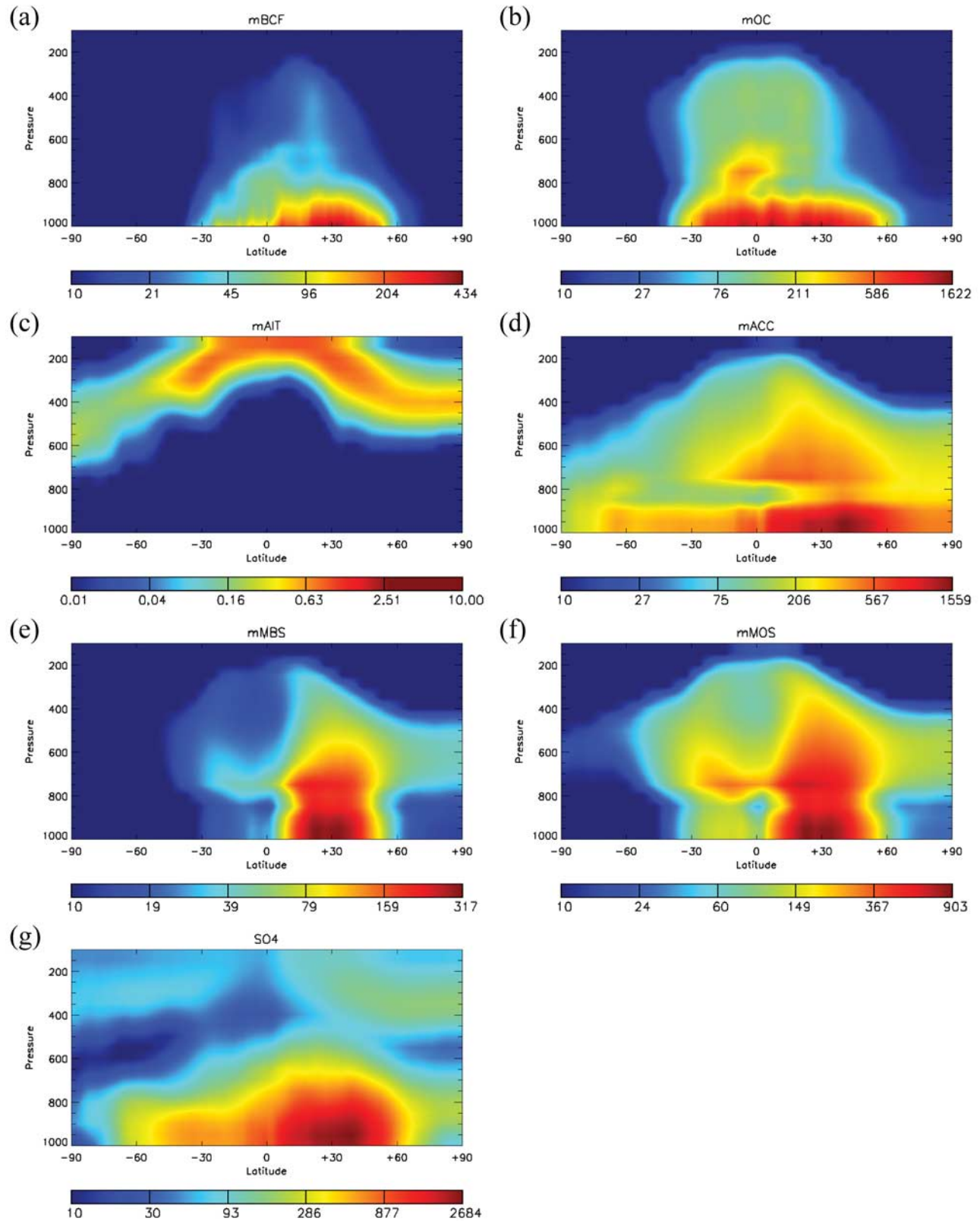
3. Aerosol Distribution and Concentrations

3.1. Distribution of Anthropogenic Aerosols

[34] The mass column loadings of all types of aerosols show their high values around the major source areas in the Northern Hemisphere due to the short residence time of these particles (Figure 4). However, each aerosol mode also exhibits its own characteristics. External BC, OC, and NUC mass generally gather around the major source regions because of their fast transformations to other modes such as MBS, MOS, or AIT as well as ACC. MBS and MOS are more dispersed downwind of the emission regions even though sharp gradients in their distributions do exist. The column loading of sulfate derived from the coexisting traditional 1-moment model (CAM3S; Figure 4g) shows a similar distribution to that of ACC in the Northern Hemisphere although with higher values than the latter, implying the role of mixed aerosols in distributing aerosol sulfate mass in the new aerosol model.
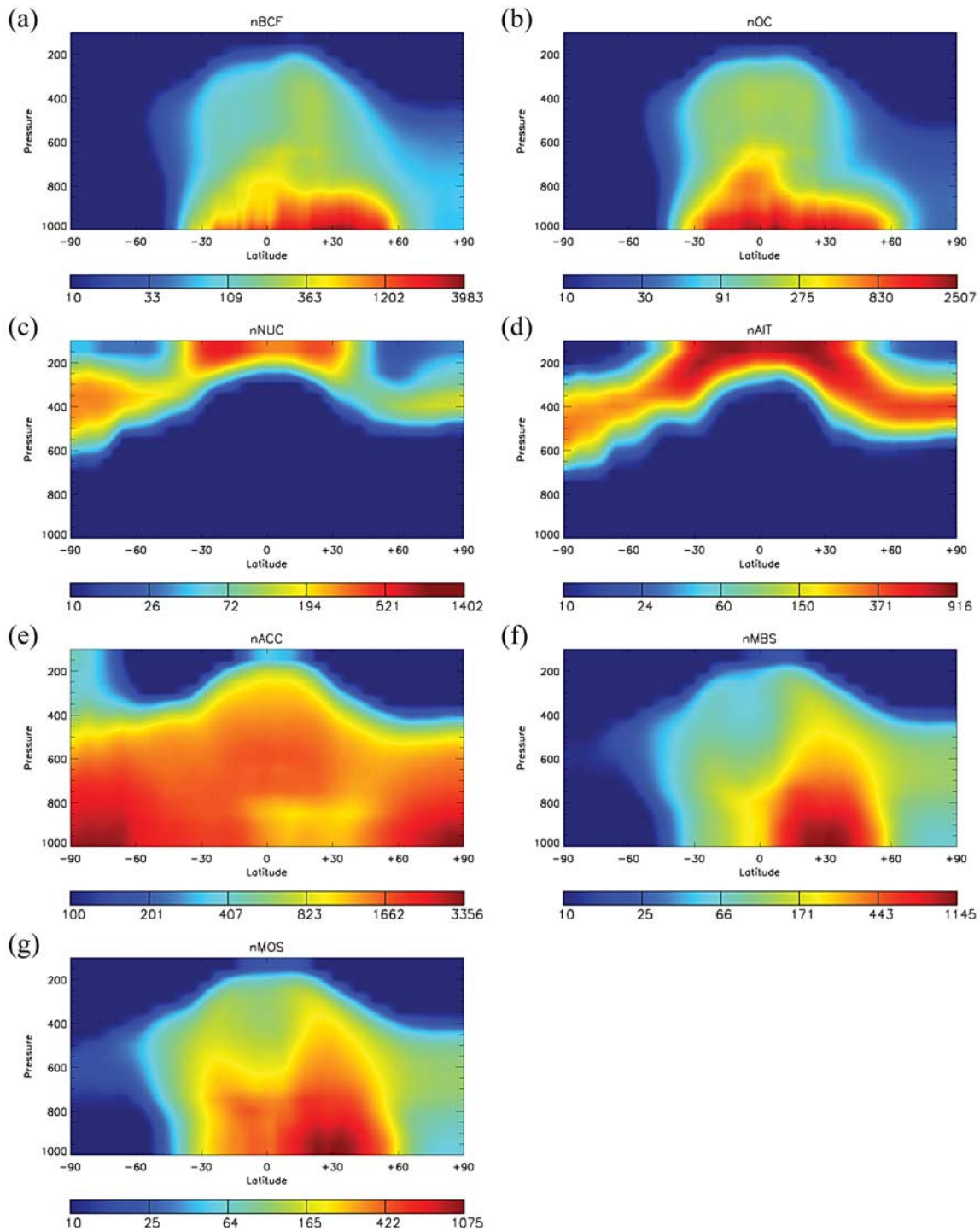
[35] The annually averaged zonal mean distribution of each aerosol type has maximum aerosol mass concentrations in the lower troposphere over midlatitude regions of the Northern Hemisphere with a sharp latitudinal gradient (Figure 5; note that OC also has a peak in the Southern Hemisphere as well). In addition, there is a strong scavenging zone over the tropics in the distributions of mixed aerosols and, to a lesser extent, of sulfate aerosols. This indicates that the tropics represents a strong barrier for the interhemispheric transport of hydrophilic aerosols emitted or formed over the Northern Hemisphere to enter the Southern Hemisphere [cf. also *Wilcox and Ramanathan*, 2004]. Considerable vertical transport up to 100 hPa is seen in the zonal mean mass distributions of OC, AIT, ACC, MBS, and MOS, primarily over the tropical area. Meridional transport of these

Figure 4. Modeled mass column loadings of (a) external BC, (b) external OC, (c) AIT, (d) ACC, (e) MBS, (f) MOS mode aerosols, and (g) sulfate mass predicted by the sulfate chemistry module in *Barth et al.* [2000]. All units are in g km^{-2} (1 g km^{-2} is equivalent to 0.001 mg m^{-2}). Note that different color scales are used for each panel. Mass of NUC is negligible and is not shown.
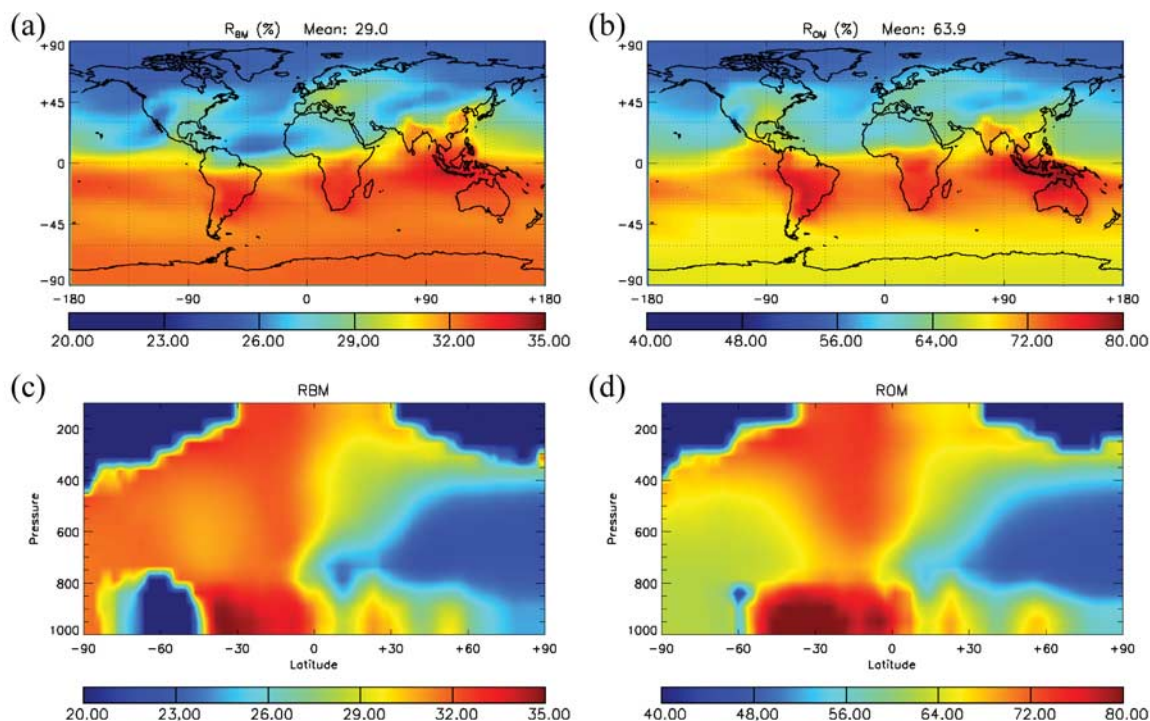
Figure 5. Modeled zonal mean mass concentrations of (a) external BC, (b) external OC, (c) AIT, (d) ACC, (e) MBS, (f) MOS mode aerosols, and (g) sulfate mass predicted by the sulfate chemistry module in *Barth et al.* [2000]. All units are in ng m^{-3}. Note that different color scales are used.

Figure 6. Modeled zonal mean number concentrations of (a) external BC, (b) external OC, (c) NUC, (d) AIT, (e) ACC, (f) MBS, and (g) MOS mode aerosols. All are in cm^{-3}. Note that the color scales are different.

aerosols in the middle and upper troposphere toward northern high latitudes can be also identified. Interestingly, AIT shows a layer of high mass concentrations in the upper troposphere. This is caused by both aerosol nucleation and convective transport of aerosols [*Wilson et al.*, 2001; *Ekman et al.*, 2006]. Note that the latter process would primarily transport aerosols directly from the lower to the upper troposphere in the climate model. In comparison, CAM3S derives a zonal mean vertical distribution in several ways similar to that of ACC including a concentrated aerosol layer close to the ground centered in the 30°N and an extended distribution into lower troposphere over high latitudes in particular in the Southern Hemisphere. The major differences between the CAM3S and ACC zonal mean mass distributions appear in the vertical layer

Figure 7. Geographical (a and b) and zonal (c and d) distributions of the black carbon mass−MBS mass ratio (R_{BM}) and the organic carbon mass−MOS mass ratio (R_{OM}). Data shown here are the column averages in percent.

corresponding to the cloud base and also middle and upper troposphere over the Southern Hemisphere due to the difference in wet scavenging processes and added interaction of ACC with other aerosols in the new model, especially in strong scavenging zones.

[36] The zonal distribution of aerosol number concentrations is shown in Figure 6. The number concentration of large particles (e.g., ACC, MBS, and MOS) gradually decreases with altitude. In comparison, the number concentrations of external BC and OC decrease with height more rapidly because of the aging process that occurs in the lower levels. Note that following the Köhler equation and using the κ value, only particles larger than activation size are removed in the nucleation scavenging process. Therefore this removal generally reduces the mass (dominated by a few large particles) rather than the number of aerosols. This is why the number concentration of ACC has not been reduced significantly in the region (500−2000 m) where substantial mass has been removed (Figures 5d and 6e). It appears that ACC number concentration is higher than expected in remote areas. The low mass concentration in these locations suggests that these are small particles. These small particles are a result of low scavenging occurring at the high latitudes, but could also be an artifact caused by the prescribed number concentration from rain and cloud droplet evaporation. Nevertheless, it does not affect the radiation calculation. Smaller sulfate particles, i.e., NUC and AIT, display high number concentrations in the upper troposphere with the peak values appearing just below the tropopause. This can be explained by the binary nucleation process included in the model that favors low temperatures

given the same sulfuric acid concentration [*Kulmala et al.*, 2000, 2004; *Wilson et al.*, 2001; *Ekman et al.*, 2004, 2006]. Unlike the aerosol modes with large size, the zonal mean distributions of the number concentrations of NUC and AIT exceed their values in the lower troposphere, opposite to their mass zonal distributions. This indicates that a large number of small sulfate particles dominate the aerosol population in the middle and upper troposphere. The feature of high concentrations of small particles in the upper troposphere is also seen in the Southern Hemisphere. A sensitivity test shows that switching the calculation of sulfate nucleation in front of condensation in the model can significantly increase the number concentrations of NUC and AIT aerosols in the upper troposphere. A similar finding is also reported by other studies [i.e., *Wilson et al.*, 2001; *Lee et al.*, 2003].

[37] The explicit prediction of BC-sulfate mixed aerosols based on a core-shell model is a unique feature of this study. Note that the mixed aerosols are treated as an individual compound so that the physical and chemical processes of MBS and MOS along with their lifetimes are significantly different than those of externally mixed sulfate, black carbon, and organic carbon. Figure 7 shows the column-integrated fraction of black carbon mass ratio in the MBS mode (R_{BM}) and that of organic carbon mass ratio in the MOS mixed mode (R_{OM}), respectively. Both R_{BM} and R_{OM} are significantly lower over the Northern Hemisphere than Southern Hemisphere, due to the higher SO_2 emission (see also Figure 2e). Apparently, the high availability of aerosol sulfate as well as sulfuric acid gas over the Northern Hemisphere result in a relatively high sulfate concentration

Table 3. Calculated Global Atmospheric Aerosol Burden (Tg or TgS)[a]

Aerosol Mode[b]	This Study (with EPPA Emissions)		Wilson et al. [2001]	Stier et al. [2005]
	EEE/ECE[c]	All Other Cases[d]		
BC	0.288	0.149	0.040	0.11
BIM	–	0.082	0.199	
MSO4	–	0.257	0.497	0.80
ACC	0.718	0.541	0.204	
AIT	2.41×10^{-3}	1.01×10^{-3}	2.51×10^{-3}	
NUC	2.17×10^{-5}	1.12×10^{-5}	3.50×10^{-4}	
OC	1.773	0.769	1.460	0.99
OIM	–	0.724		

[a]BIM and OIM are black carbon and organic carbon in MBS and MOS, respectively. MSO4 (TgS) represents sulfate in MBS and MOS. Data of this study are derived using 3-year means.

[b]Note that total sulfate burden derived with the single mode sulfate chemistry model in Barth et al. [2000] (CAM3S) is 0.678 TgS and total BC loading in Wang [2004] is 0.17 Tg.

[c]There are no mixed aerosols in EEE and ECE runs, and the chemical compounds are externally mixed.

[d]All other cases include EEA, ECA, and EHA runs.

in these mixed aerosols due to both condensation of sulfuric acid on these aerosols and the coagulation of mixed aerosols with the sulfate modes. Over the Southern Hemisphere, the values of R_{BM} and R_{OM} are higher over land than over ocean, indicating the effects of emissions of primary carbonaceous aerosols and the formation of secondary OC, added by the significant reduction of sulfate aerosols and sulfuric acid gas by tropical precipitation that inhibits the sulfate entering the SH from the NH. The distinctive hemispheric differences of R_{BM} and R_{OM} can be also seen in their zonal mean distributions (Figures 7c and 7d).

[38] The global average column-mean R_{BM} is about 29.0%, which is higher than the range between 2% and 14% used in previous studies [e.g., Haywood and Shine, 1995]. The geographical distribution and global atmospheric burden of total black carbon (external BC + BC in MBS) is larger than that derived in Wang [2004]. With a global mean of 63.9%, however, the value of R_{OM} is much higher than R_{BM}. This is caused by the large amount of secondary organic carbon aerosols in particular over the SH. The global atmospheric burden of the seven aerosol modes has been compared with two similar previous studies (Table 3). The total loadings of sulfate derived by all three models are in good agreement. The total loadings of carbonaceous aerosols by our model are similar to those in Wilson et al. [2001], but both

are significantly higher than that derived by Stier et al. [2005]. Note that the BC emission used in the latter study is only about half of that of EPPA estimation. Interestingly, we have found that the total aerosol mass of BC and OC in the ECE run that prohibits mixtures is 24.7% and 18.8% higher than that in ECA run, respectively. The total aerosol sulfate in ECE run, on the other hand, is 10.1% lower than ECA results. Therefore inclusion of mixed aerosols in the model leads to a stronger sink of carbonaceous aerosols and a weaker sink of sulfate due to the different rate of nucleation scavenging as a function of aerosol hygroscopicity, implying the important effect of mixing state in aerosol constituent abundance.

[39] With a constant aging timescale of 40 hours, about 35.5% of black carbon mass is in the MBS mode (0.082 Tg of BC in MBS mode vs. 0.139 Tg in external BC). This ratio is quite different than that found in Wilson et al. [2001], which was 0.199 Tg of BC in mixed mode and 0.040 Tg in external BC. The difference most likely arises due to the sulfuric acid limitation applied to the aging calculation in our model. The model predicted fraction of internally mixed black carbon agrees reasonably with recent observations over Costa Rica (1°S–10°N, 80–85°W) which displayed a range between 30 and 40 % in the troposphere, except for the boundary layer [Schwarz et al., 2008]. In comparison, the mass distribution of organic aerosol is different than that of black carbon in our

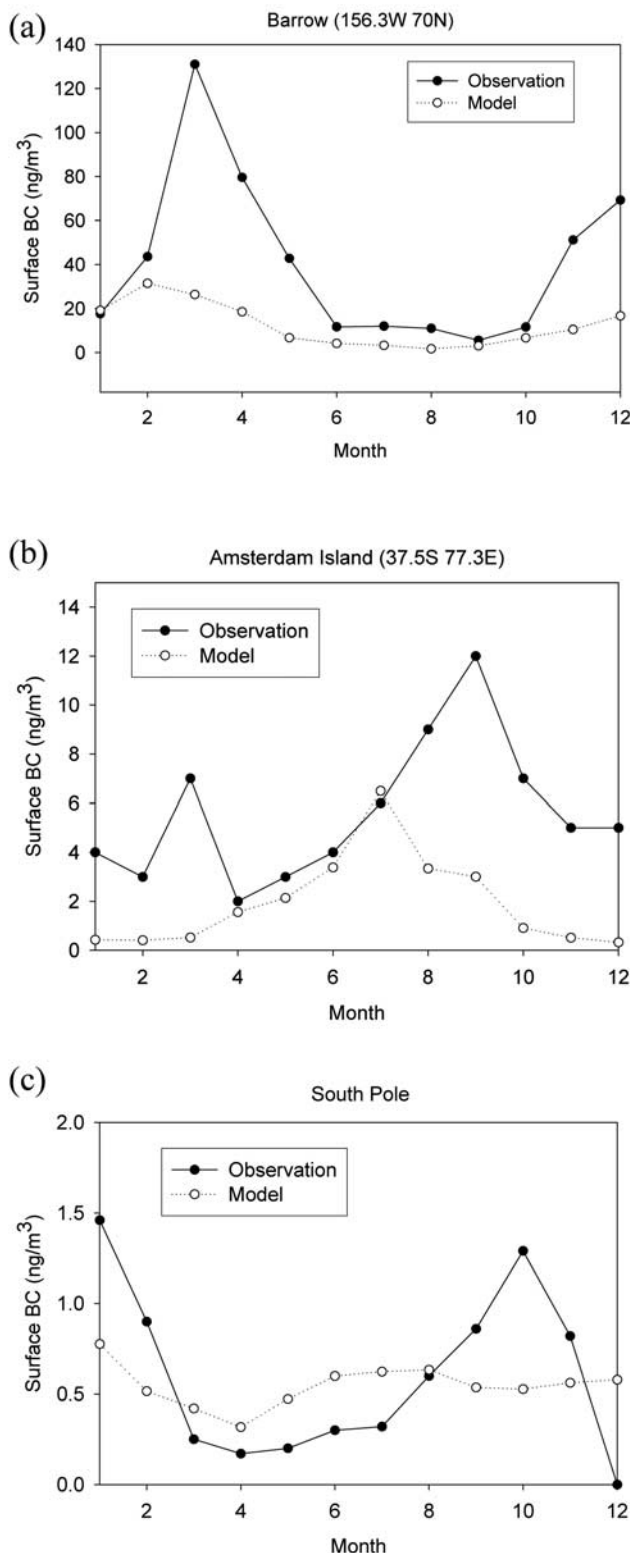**Table 4.** Global Mean Aerosol Mass Budget From EEA, ECA, and EHA Runs (%)[a]

		BC	OC	NUC	AIT	ACC	MBS	MOS	BIM	OIM	H₂SO₄
Source	Emission	100.0	100.0								
	Nucleation			0.6							
	Oxidation					99.0					100.0
	Aging						25.3	54.4	100.0	100.0	
	Condensation			99.4	86.7	1.0	47.3	12.5			
	Coagulation				1.4	0.0	27.3	33.1			
	Growth[b]				11.9	0.0					
	Total	100.0	100.0	100.0	100.0	100.0	100.0	100.0	100.0	100.0	100.0
Sink	Scav (Dry)	22.8	10.7	0.0	0.0	9.3	9.9	8.4	10.6	8.9	0.0
	Scav (Imp)	37.3	33.3	1.7	0.3	21.6	46.2	42.7	46.3	42.6	0.0
	Scav (Nucl)		15.7		0.0	60.1	43.9	48.9	43.1	48.5	
	Aging	39.9	28.9								37.5
	Condensation										62.5
	Coagulation		11.4	14.0	57.4	9.0					
	Growth[b]			84.3	42.3						
	Total	100.0	100.0	100.0	100.0	100.0	100.0	100.0	100.0	100.0	100.0

[a]Data are derived using 3-year means.

[b]The estimated life times of black carbon, organic carbon, and sulfate are 10.7, 12.6, and 9.6 days, respectively.

[c]Sulfate mass moves to the larger mode when the size of particles are larger than the upper limit of defined mode.

Figure 8. Comparison of observed and model simulated black carbon mass concentrations at three stations: (a) Barrow, (b) Amsterdam Island, (c) South Pole. Three-year averaged values are used for the simulations. Observation are from *Bodhaine* [1995] and *Liousse et al.* [1996].

model. The mass fraction of OIM (compared to total organic carbon mass) is about 48.5%, which is substantially larger than the case of BC because of the faster aging time. The most dominant sulfate mode in our model is ACC which possesses 67.7% of the total aerosol sulfate mass. Most of the remaining aerosol sulfate mass (32.2%) is present in the two mixed modes (0.085 TgS in MBS and 0.175 TgS in MOS). Note that the global aerosol sulfate burden derived by our model is larger than the CAM3S result due to different microphysics as well as the wet and dry removal processes adopted in the new aerosol model.

[40] The mass budgets of all aerosol modes are calculated and shown in Table 4. The atmospheric abundance of hydrophobic external BC is balanced between emissions and sinks including dry deposition, impaction scavenging, and the aging process. Specifically, the aging process accounts for nearly 40% of the mass loss of external BC. Including the MBS mode in the model is found to reduce the total black carbon aerosol mass in the atmosphere compared to the result of a sensitivity run using the all-external BC model (0.231 vs. 0.269 or a 14% reduction). This is attributed to the shorter lifetime of MBS in the new aerosol model due to nucleation scavenging. For the external OC, the largest sink is the impaction scavenging (33%), followed by aging (29%), nucleation scavenging (16%), and dry deposition (11%). Condensation is the major mass source of the smaller external sulfate aerosols (NUC and AIT). The growth in size by intermode coagulation and condensation (i.e., growth in the table) of these particles and the subsequent transfer into the larger mode sizes (i.e., NUC to AIT and AIT to ACC) is the most important sink term (the largest for NUC and second largest for AIT). Intermode coagulation of AIT sulfate with MBS and MOS constitutes the largest sink for AIT while the second largest source for both MBS and MOS. Aqueous phase oxidation is found to be the most dominant source of ACC mass. The source is in general balanced by the mass loss through nucleation scavenging (60%) and in much smaller quantities by the impaction scavenging and dry deposition. For the two mixed modes, condensation, coagulation, and aging processes are all important sources while the wet removal processes dominate their sinks. Note that the aging rate of OC, which is twice as fast as that of BC, results in a much larger relative contribution in OC abundance compared to the case of BC.
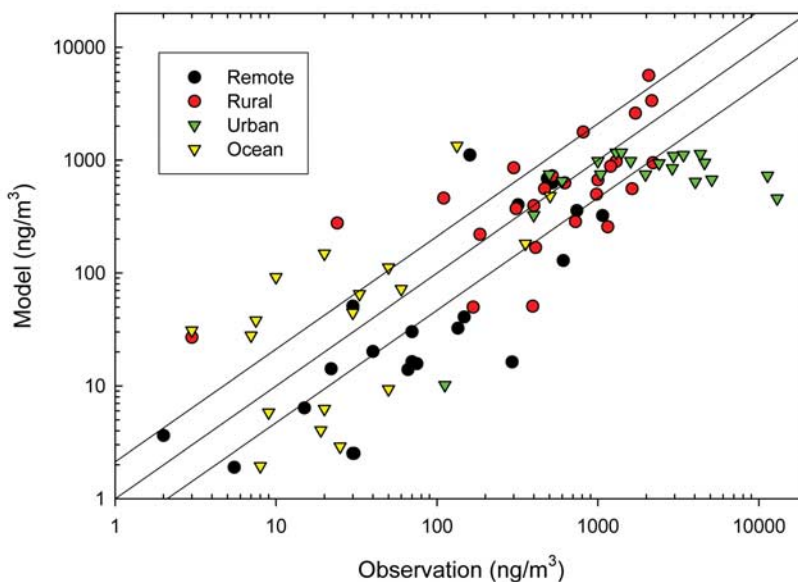
3.2. Comparison of Modeled Results With Observations

[41] Since most observed aerosol mass concentrations are given as the mass of a given chemical compound such as black carbon, organic carbon, or sulfate, model-predicted aerosol mass concentrations are regrouped into corresponding aerosol constituents in the comparison following equation (7). When comparing the model results to surface station measurements, the nearest model grid to the measurement site is chosen. Note that although the comparisons are made specifically using ECA output, the result is also representative for the EEA and EHA run.

3.2.1. Black Carbon Mass Concentration

[42] Figure 8 shows the comparison of model simulated monthly mean surface mass concentration of black carbon versus selected observations in remote regions. Model

Figure 9. Observed and simulated black carbon mass concentrations at multiple surface sites. Observation data are obtained from various field measurements [*Liousse et al.*, 1996; *Cooke et al.*, 1999]. Three-year averaged values are used for the simulations.

captures the lower concentration season (summer) but generally underestimates in spring and winter season at the Barrow station. At Amsterdam Island (located in the Indian Ocean), the modeled BC mass does not show the same strong seasonal cycle as that seen in the observations. The modeling study by *Wang* [2004], which used a single moment aerosol scheme, also underpredicted BC during summer at Amsterdam Island. At the South Pole, where BC mass is extremely low, the modeled BC mass concentration agrees fairly well with observations except for an overestimate in the later part of the year.

[43] Figure 9 shows a comparison of modeled results with a number of derived BC mass concentrations from optical measurements which range from a few ng m^{-3} to a few thousand ng m^{-3} [*Liousse et al.*, 1996; *Cooke et al.*, 1999]. Over locations with BC mass concentration between 600 and 3000 ng m^{-3} (largely rural and urban sites), the model results mostly agree with the observation within a factor of two. The model-observation correlation appears scattered in locations with BC mass concentration lower than 600 ng m^{-3}. For sites where very high BC mass concentrations are measured (mostly urban locations), the model underestimates the observations because of the coarse resolution of the model in comparison to the size of urban centers or pollution plumes. It is interesting to note that some differences exist in surface BC mass concentration between the present modeling result and *Wang* [2004], which used single moment BC model, even though both studies used the same BC emission inventory of EPPA. The different climate models (CCM3 in *Wang* [2004] and CAM3.0 in this study) as well as the aerosol processes included in these two models, especially the transfer of BC to MBS included in this study, are the reasons for the differences in modeled BC mass distributions between the two studies.
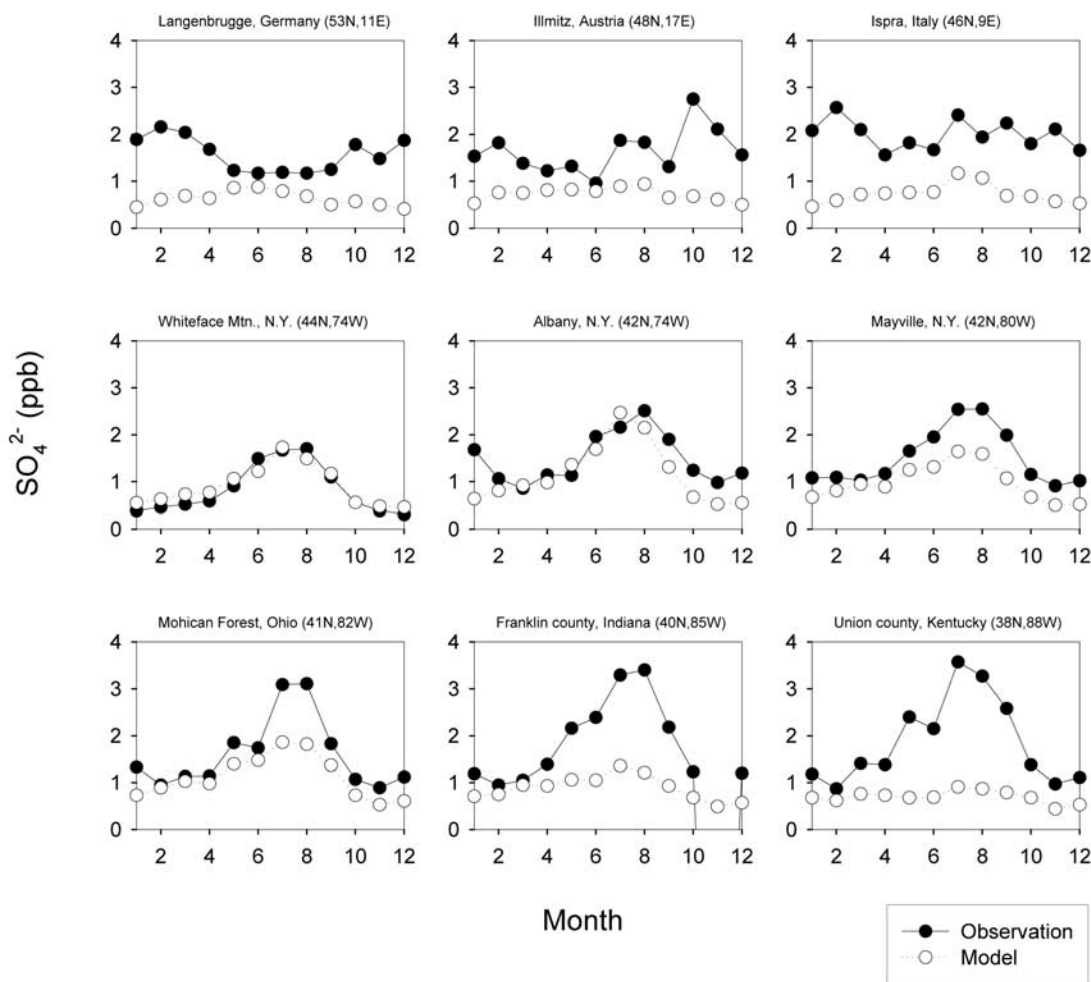
3.2.2. Sulfate Mass Concentration

[44] Simulated values of monthly mean surface sulfate mass concentration are compared with observations at vari-

ous locations over the globe (Figure 10). The magnitude of modeled and measured sulfate mass is similar for most midlatitudinal US and European stations, corresponding to areas with overall high SO$_2$ emissions (Figure 10a). A strong seasonal cycle with a summer peak is seen in the observations at US sites while it is not as apparent at three European stations. The model captures both the seasonal cycle and the absolute magnitude of the observations at US sites except for Franklin County, Indiana (40°N, 85°W) and Union County, Kentucky (38°N, 88°W). For the European sites, the modeled annual average surface mass concentration of sulfate appears to be about factor of two lower than observations.

[45] At Arctic and sub-Arctic sites (Figure 10b), the major source of both SO$_2$ and sulfate is from transport. Surface sulfate mass concentration has a peak during the months of March, April, and May (MAM) and a low during the months of June, July, and August (JJA) due to the general circulation pattern which gives the strongest transport from lower latitudes during spring. The model does capture the seasonality and thus the simulated mass concentrations agree reasonably well with observations at these sites. However, the modeled peak values during MAM are clearly lower than observations. For oceanic stations (Figure 10c), simulated sulfate mass concentrations are found to agree well with observations regarding seasonality and are within a factor of two of the observed magnitude.

[46] The model-simulated seasonal means of surface sulfate mass are compared with measurements conducted at monitoring stations over the United States and Europe (Figure 11). The US data are for year 2000 from the US EPA Clean Air Status and Trends Network (CASTNET) (http://www.epa.gov/castnet/data). The 3-year averages of 2000–2002 from the Evaluation of the Long-Range Transmission of Air Pollutants in Europe (EMEP) database (http://www.nilu.no/projects/ccc/emepdata.html) are used for Europe. The measured concentrations range between 0.4–20 μg m^{-3} in the US and 0.1–6 μg m^{-3} in Europe. The

Figure 10. (a) Comparison between observed and model simulated surface sulfate mass concentrations at midlatitudinal U.S. and European stations. (b) Comparison between observed and model simulated surface sulfate mass concentrations at Arctic and sub-Arctic stations. (c) Comparison between observed and model-simulated surface sulfate mass concentrations at several oceanic stations. Observational data were compiled by *Barth et al.* [2000]. Modeled results are 3-year means.

comparison result suggests that the model underestimates surface sulfate mass over the US while capturing well the observations over Europe throughout the year. The underestimate for US stations occurs for both very high and very low sulfate concentration cases. Therefore it is likely attributed to the model resolution (note that modeled results represent averaged values over the area of a grid; see also Figure 10). In addition, any model error in predicting rainfall over the US and Europe could contribute to the above discrepancy as well [i.e., *Rasch et al.*, 2000; *Hack et al.*, 2006].

[47] Vertical profiles of sulfate mass concentration measured with an aerosol mass spectrometer onboard the research airplane Twin Otter during the Aerosol Characterization Experiment (ACE-ASIA, spring of 2001; *Bahreini et al.*, 2003) are compared to the model results (Figure 12a). The measurements were made on flights near Japan ($127\sim135°$E and $32\sim38°$N). Mean concentrations during the constant elevation (circles) flights are presented. The measured sulfate concentrations decrease with height but the wide

distribution suggests that episodic and small-scale polluted plumes frequently affect this region. Modeled April mean concentrations over the grid points corresponding to the measurement area are used for comparison with the observations. The range of modeled sulfate mass appears to be well within that of the measurements at all vertical layers from the surface to 4 km altitude. Several measurements are substantially higher than the modeled results within the vertical layers between 800 and 1200 m. These high values are most likely related to episodic pollution plumes.

[48] Vertical distributions of the modeled sulfate aerosol mass concentrations are also compared to the aircraft measurement data from three NASA Pacific Exploratory Missions, i.e., PEM-West A, PEM-West B, and PEM-Tropics A (Figure 13). Even though the aircraft data might not represent the aerosol climatology over the grid size of our model and a monthly mean time frame [e.g., *Barth et al.*, 2000], the comparison shows some general agreement between the two. It shows good agreement in most cases
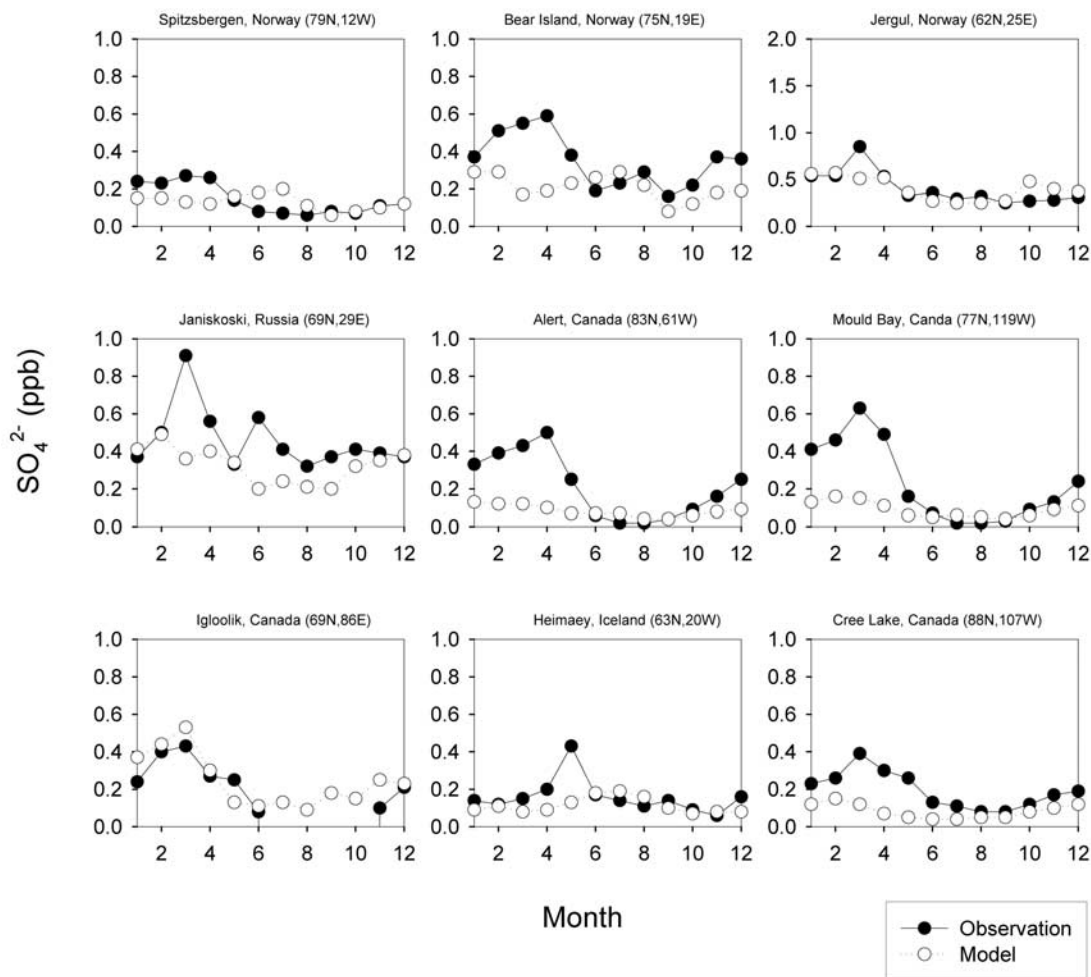
Figure 10. (continued)

between modeled and observed data in the middle and upper troposphere even over remote and oceanic regions (i.e., Easter Island, Guam, Guayaquill, and Fiji). However, the model does not reproduce the observed high variability of sulfate mass, especially in the lower troposphere. The high values of observed sulfate are most likely caused by either local emissions of sulfate or by air pollution plumes, which horizontal extent should be considerably smaller than the model grid cell (e.g., for Japan and Hong Kong measurements during PEM-West B and Guayaquill measurements during PEM-Tropics A).

3.2.3. Organic Carbon Mass Concentration

[49] Modeled surface organic carbon concentrations show good agreement with observations from the EPA stations over the US, in contrast to the case of sulfate, while the comparison with observed values from the EMEP network in Europe appears to be more scattered and frequently an underestimate (Figure 14). In addition to the comparison with station data, vertical OC distribution is compared with the data from ACE-ASIA field experiment (Figure 12b). The vertical distribution shows a strong vertical gradient of OC mass concentration above the boundary layer. Measured OC varies widely between nearly 0 and 4 $\mu g\ m^{-3}$ STP in an upper atmospheric layer above 2800 m, implying an influ-

ence of polluted plumes during the measurements. Except for this elevated layer the model predicted OC mass concentrations are well within the range of measurements.

3.2.4. Aerosol Size Distribution and Number Concentration

[50] Model simulated monthly aerosol number concentrations are compared with the aerosol number concentration data measured at multiple northern hemispheric stations within NOAA/ESRL (http://www.esrl.noaa.gov/gmd/aero/net/index.html). In these measurements, aerosol number concentration is determined with a CN counter and the lower detection limit of the instrument is 10 nm in diameter. The model predictions agree with the measurements within a factor of two at most stations (Figure 15). Modeled results show a summer high at most sites except Barrow and Kosan due to the more effective aerosol production and also the general circulation pattern. Considering the very high aerosol number concentrations at some stations (i.e., Bondville and Kosan), the discrepancy between modeled results and measurements at these stations is most likely due to the local sources.

[51] Aerosol size distribution data from the Norsk Institutt for Luftforskning online database of the Construction, Use and Delivery of a European Aerosol Database (CREATE)
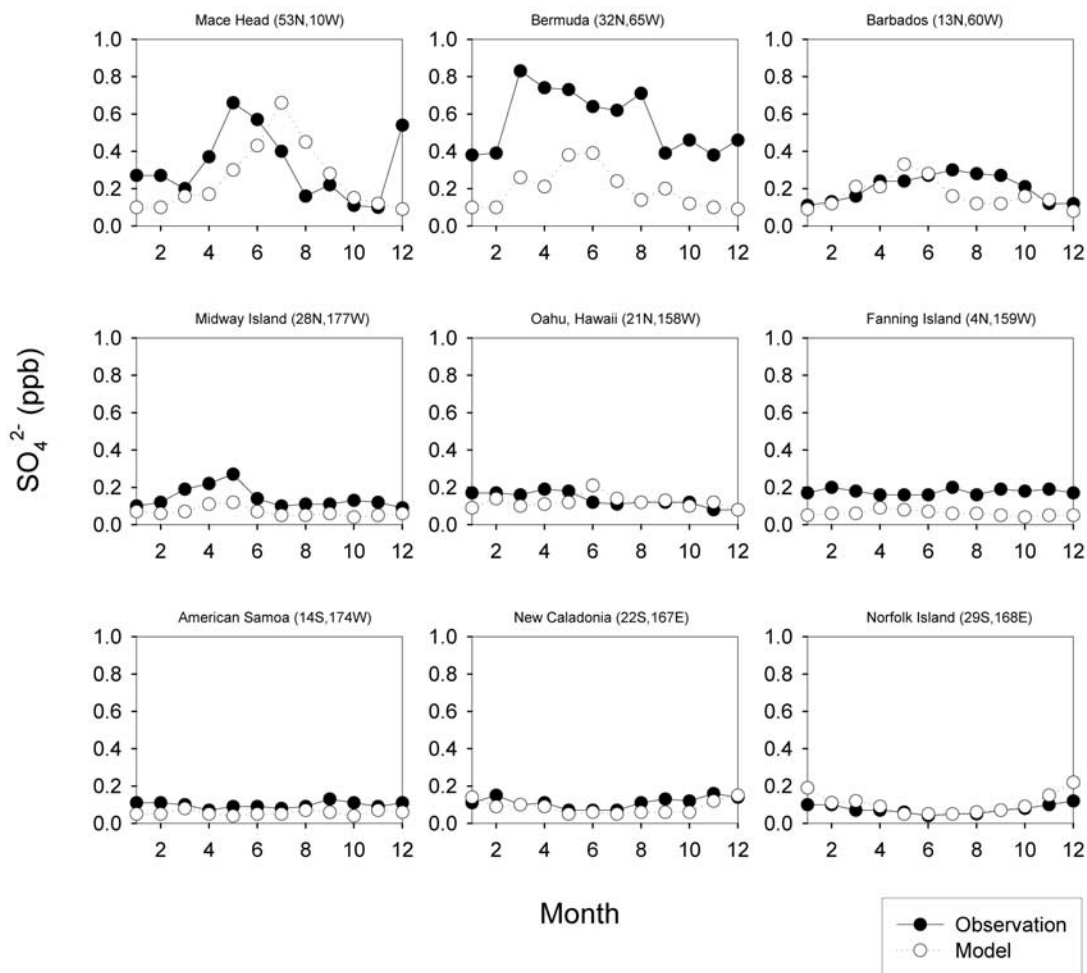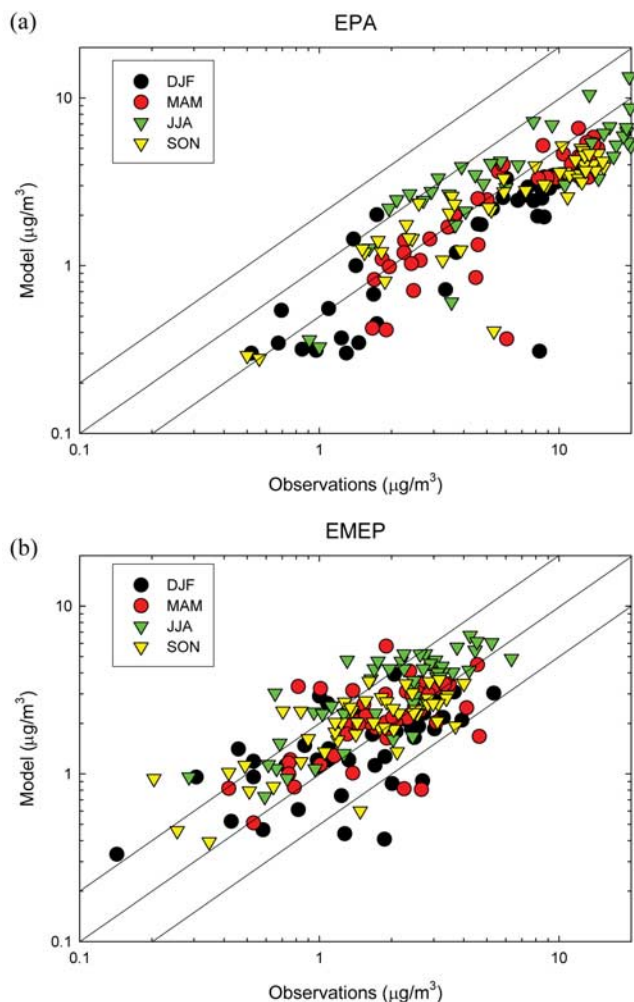
Figure 10. (continued)

project (http://www.nilu.no/projects/ccc/create/database.htm) are also used in the comparison with model predictions. These data were measured at several EMEP stations in Europe for a size range between a few nm to 800 nm. The instrumental detection limit of these observations varies among different sites, ranging from 3 nm to 20 nm in diameter. The data are averaged into annual means. As the observational results represent the total number of various aerosol types and composition including sulfate, carbonaceous, nitrate, dust, and perhaps sea salt, we have combined the modeled number concentrations of external carbonaceous, mixed, and external sulfate aerosol modes in each corresponding size bin of the aerosol observations in the comparison. The modeled aerosol size distributions are found to follow the observations rather well except in the smallest size range (Figure 16). Modeled number concentrations are generally lower than the observations. A few factors might contribute to this discrepancy. Firstly, our model only includes sulfate and carbonaceous aerosol constituents while observed aerosols also contain other aerosol constituents such as ammonia, nitrate, mineral dust, and sea salt. Secondly, the horizontal model resolution is larger than 200 km and clearly this is too coarse to resolve certain local events with high aerosol number concentrations. Neverthe-

less, the differences between modeled and observed results are generally within an order of magnitude.

[52] Several aircraft measurements of two aerosol size ranges were made during the TRAnsport and Chemical Evolution over the Pacific (TRACE-P) mission. During the flights, a Differential Mobility Analyzer (DMA) and an Optical Particle Counter (OPC) were deployed to measure aerosol numbers in two different aerosol diameter ranges of 7–100 nm and 100–750 nm, respectively. In order to directly compare the modeled results with these measurements, modeled aerosol number concentrations in various modes corresponding to the two size ranges of the measurements have been derived first for each mode and then summed together. The comparisons show (Figure 17) that for the smaller size bin, the model results agree rather well with observations over Hong Kong and Japan, while the model results are higher than observations over Guam. For all three sites they modeled concentration of smaller aerosols are mostly within the range of the observed variability (Figure 17, left column). For the large particle size range, the model captures the "background" and upper tropospheric measurements. However, for the regions (Japan and Hong Kong) that are constantly under the influence of episodic plumes the model misses the high concen-
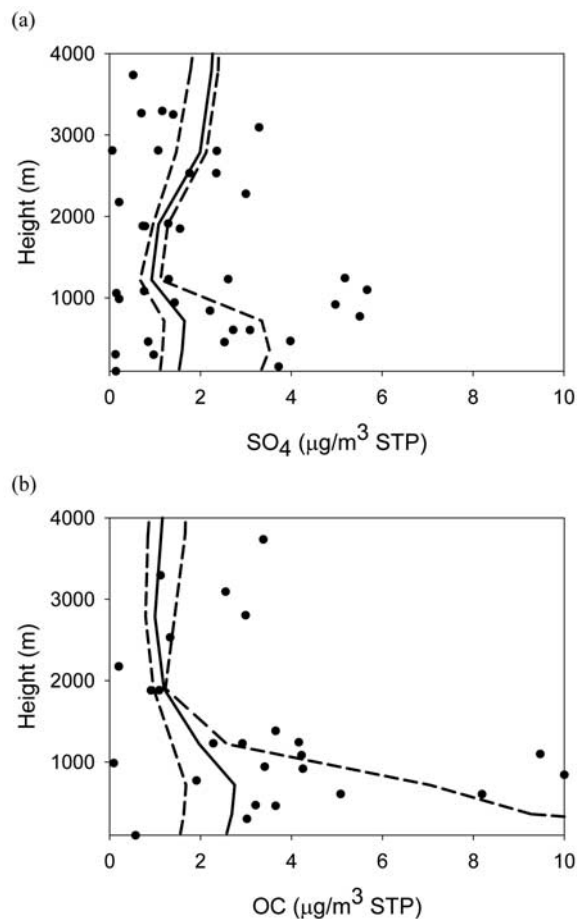
Figure 11. Comparison between observed and model-simulated seasonal means of sulfate aerosol mass concentrations at multiple stations in (a) United States and (b) Europe. Three-year averaged values are used for the simulations.

and grid points that overlap with the flight paths are selected in the comparison. CARIBIC data at altitudes between 8 and 12 km are vertically averaged along the flights and the model results are averaged over three layers around 10 km. Both data are converted to the concentration under the standard atmosphere (STP; i.e., 1013.25 hPa and 273.15 K). The first four flights are in winter months (November and December) and the others are in summer months (July and August). The source of these submicron particles is either nucleation or transport from the lower atmosphere [*Hermann et al.*, 2003; *Heintzenberg et al.*, 2003]. The modeled results are generally slightly lower than the observations but well within the error range of the observations, demonstrating that the model captures the seasonal variation of the upper tropospheric number concentration of the larger submicron aerosols (18 nm < D < 1.3 μm) observed from the CARIBIC measurements reasonably well.

[54] Similar results are obtained for a comparison of modeled results with another set of observational data [*Minikin et al.*, 2003], where the modeled number concentration of large particles (100–1000 nm) is in a good

Figure 12. Observed and simulated vertical profiles of sulfate and OC aerosol mass concentrations. Observation data are obtained from the ACE-ASIA campaign in 2000. Dots represent the mean concentrations during the constant flight height [*Bahreini et al.*, 2003]. Averaged (solid line), minimum, and maximum (dashed lines) model results are derived from a 3-year average in April.

tration events in the lower troposphere which is expected. At the Wake Island-Guam site, the model overestimates the large particles in the upper atmospheric layer, a region often dominated by the long range transport from the East Asia.
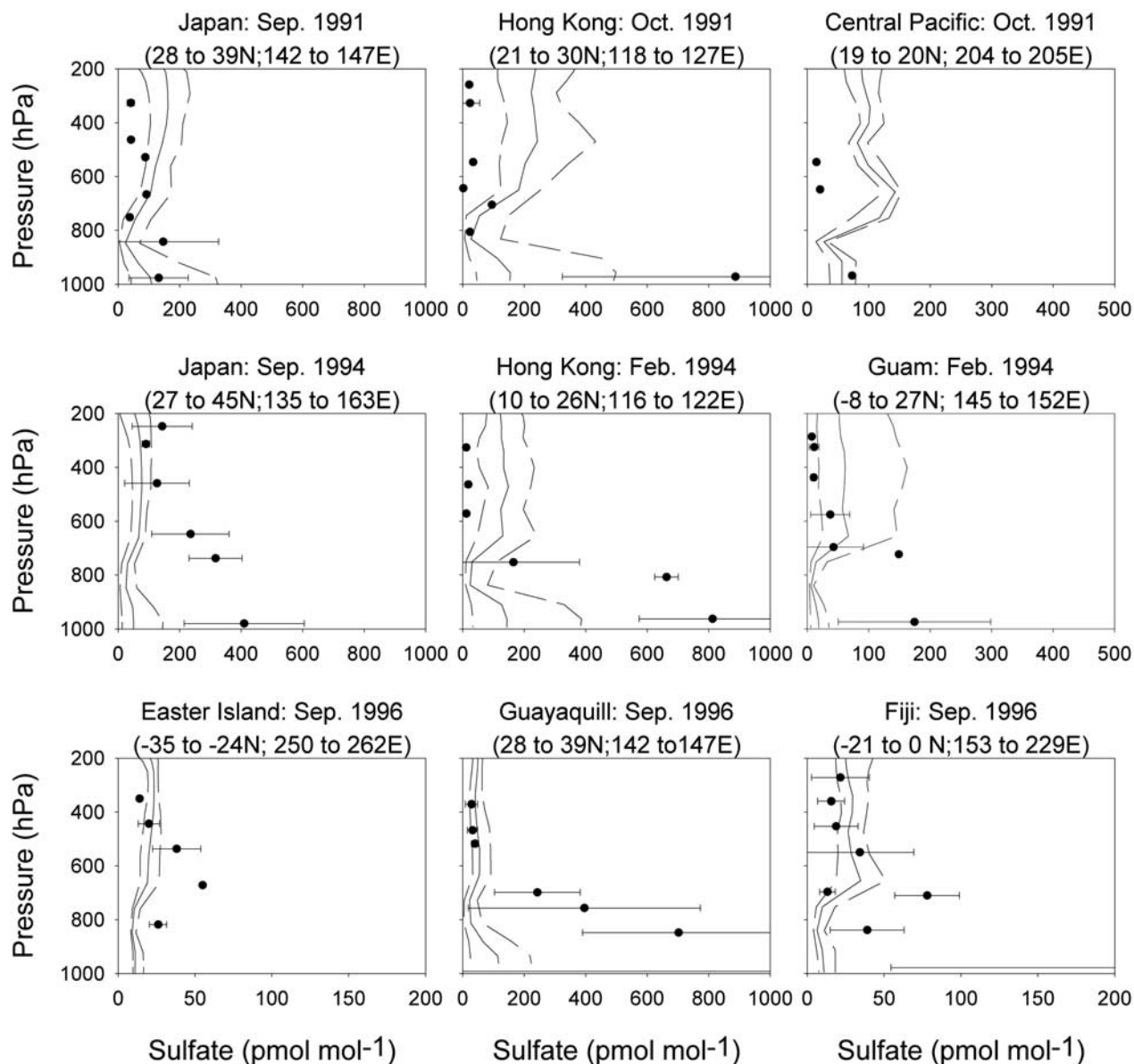
[53] The model-predicted aerosol number concentrations in the upper troposphere are further compared with the aircraft observations from the project of Civil Aircraft for Regular Investigation of the Atmosphere Based on an Instrument Container (CARIBIC) [i.e., *Hermann et al.*, 2003]. In the CARIBIC project, three Condensation Particle Counters (CPCs) were deployed on commercial aircrafts to measure aerosol (condensation nuclei) number concentrations with different lower threshold diameters (4, 12, and 18 nm). The aerosol number concentrations measured in three size ranges, i.e., 4 nm < D < 12 nm, 12 nm < D < 18 nm, and 18 nm < D < 1.3 μm, are thus used for comparison with modeled results (Figure 18). All selected flights have similar paths in the route between Germany and South India (5.2~51°N; 8.1~79°E). The modeled monthly mean results of the Aitken and accumulation external sulfate as well as the two mixed modes in corresponding months

Figure 13. Sulfate mixing ratio versus height for the different locations. Symbols are observation data obtained from PEM aircraft field programs of (a) PEM-West A, (b) PEM-West B, and (c) PEM-Tropics A [*Barth et al.*, 2000]. Observations are averaged at every 100 hPa. Solid lines are mean model results; dashed lines are maximum and minimum model-predicted monthly mean values at given model layer in the region.
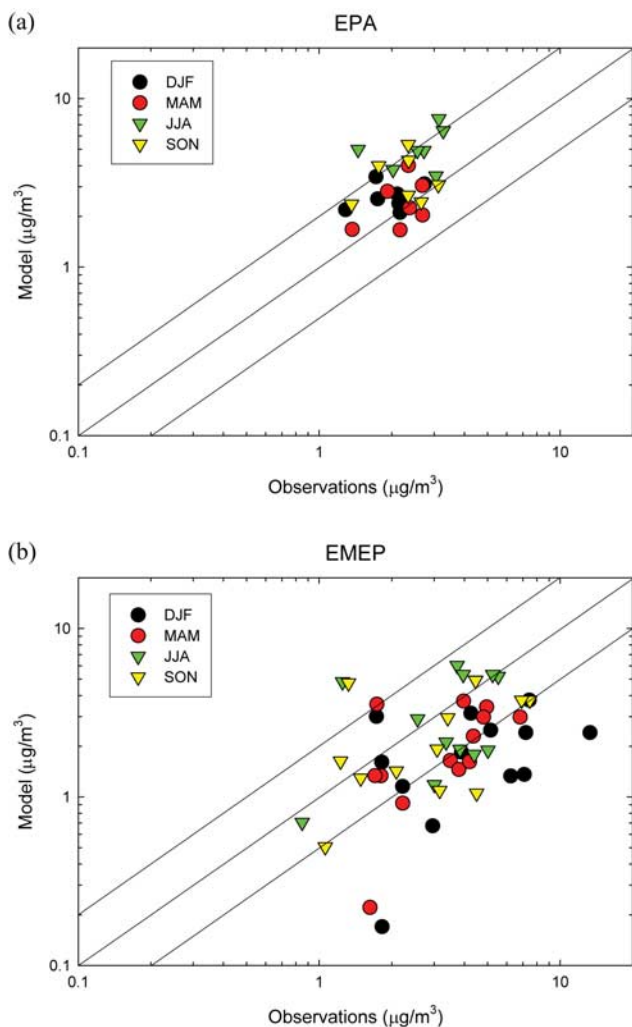
agreement with the observations (Table 5). However, the modeled number concentration of Aitken mode aerosols is about a factor of 7 larger than the observations in median value and clearly biased toward higher values even over the Northern Hemisphere. Possible reasons for the higher AIT aerosol number concentration produced by the model are either an overestimation in aerosol nucleation in the upper troposphere or an underestimation in the scavenging of the Aitken mode size aerosols.

[55] We have collected several measurements of surface number concentrations in the submicron size range from the literature and compared them with the modeled results (Table 6). Note that the measured particle size ranges

correspond to the nucleation mode and the small size part of the Aitken as well as mixed mode in our model. The model predictions at most sites are well within a factor-of-two range from the measurements. However, model overestimation appears at the Antarctic sites where low number concentrations of aerosols are often measured.

3.3. Aerosol Optical Depth (AOD)

[56] Global averaged AOD values of different modes of aerosols are listed in Table 7. For the wavelength band of 350–640 nm, sulfate (e.g., 0.0572 in EEA and 0.0195 in ECA) is the most dominant mode of anthropogenic AOD. AOD values of OC and BC are much lower in compar-

Figure 14. Comparison of observed and model simulated organic carbon mass concentrations at multiple stations in (a) United States and (b) Europe. Both primary organic aerosols (POA) and secondary organic aerosols (SOA) are included for model predictions. Modeled results are 3-year means.

ison. The difference between runs with different size distributions but the same mixing configuration (i.e., EEA vs. ECA and EEE vs. ECE) is much larger than that between runs with different mixing configurations but the same size distribution (i.e., EEA vs. EEE and ECA vs. ECE). This demonstrates that in determining the AOD of external sulfate aerosols, the size distribution is more important than mixing state. In comparison, the mixing configuration is found to be more critical than size distribution to the AOD of carbonaceous aerosols. Specifically, the AOD values of BC in 1-moment and 2-moment are essentially the same. The effect of mixing state in carbonaceous aerosol AOD is further demonstrated in the comparison between ECA and ECE runs (Table 7). The total AOD of carbonaceous aerosols is larger in ECA (also EHA) run than in ECE run due to the added shell of sulfate, despite the fact that the total carbonaceous aerosol mass is lower in the former than the latter case. When mixtures are included in the model, the AOD of MBS is

not significantly different whether calculated using the well-mixed model (i.e., volume weighted refractive indices; 0.00398) or the core-shell model (0.00395).

[57] The 1-moment method adopts only a given geometric size for each aerosol mode in calculating its optical properties and thus radiative forcing. Note that the predefined sizes of BC (11.8 nm) and SO_4 (50 nm) for the 1-moment method are frequently used in other studies and the predefined particle size of OC (20 nm) is close to the estimated global mean radius in the lower atmosphere (24 nm). Nevertheless, our results suggest that the large temporal and spatial variation of particle size makes it difficult to determine a representative size for a given type of aerosols over the globe in particular for external sulfate in our case.

[58] To compare the modeled AOD with other modeling results, we used the median value derived from 16 models of the AeroCom model intercomparison project [*Texter et al.*, 2006; *Kinne et al.*, 2006; *Schulz et al.*, 2006; Table 7] and also results produced by the GOCART model constrained by MODIS satellite data [*Chin et al.*, 2002; Y. Kaufman and M. Chin, personal communication, (2005)]. We found that our results obtained using the 1-moment external mixture scheme (Run EEA) is about 67% higher than the median values of AeroCom models but very close to the GOCART data. The results derived using the 2-moment scheme (Run ECA) agree well with the median values of AeroCOM models while they are about 36% lower than GOCART data.
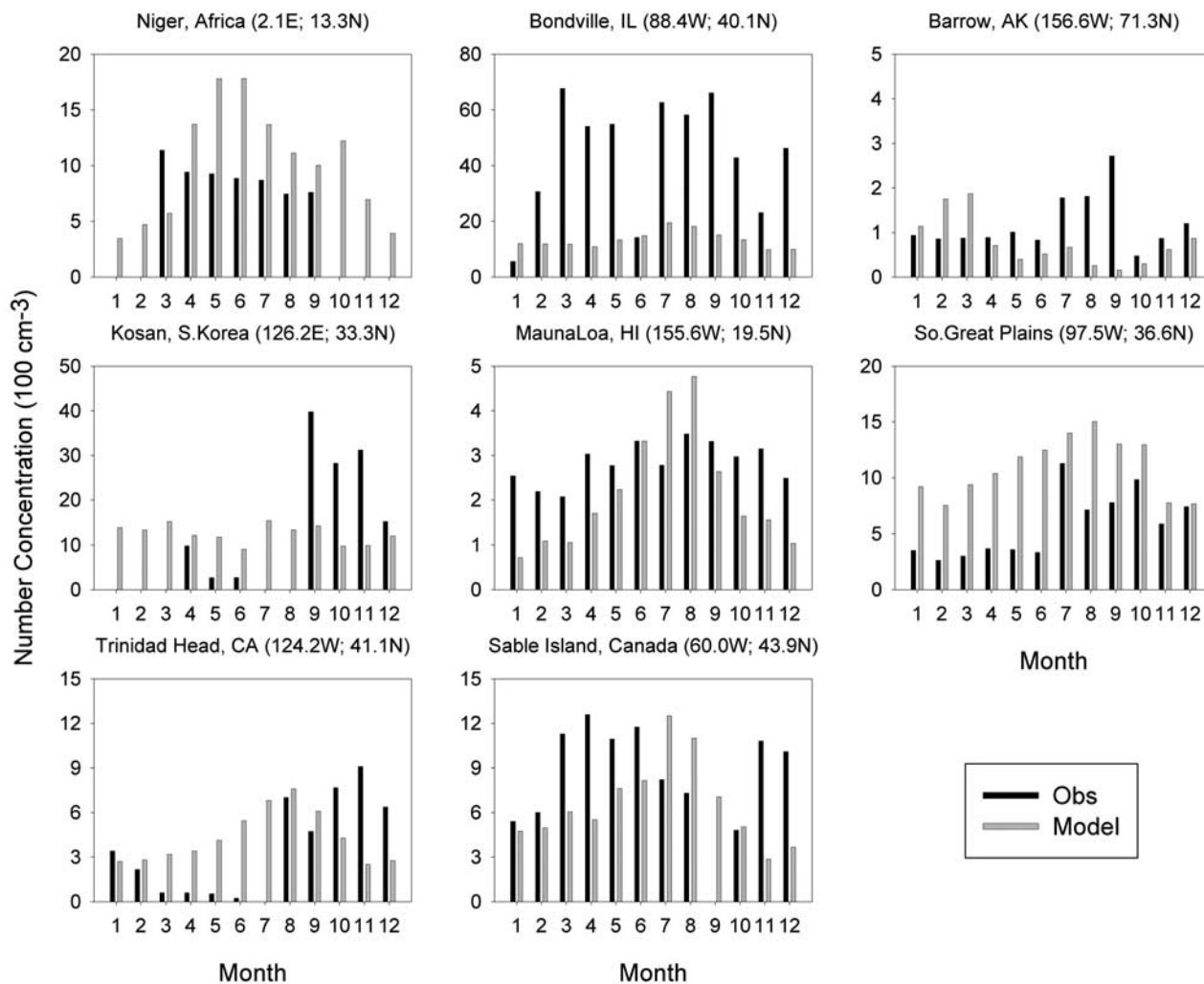
[59] In addition to the AeroCom and MODIS-GOCART AOD comparison, the modeled AOD are compared with the surface measurements from the Aerosol Robotic Network (AERONET, http://aeronet.gsfc.nasa.gov/) (Figure 19). Seventy six AERONET sites were selected to represent various regions over the globe. The modeled aerosol optical depth at the wavelength ranges of 350–640 nm is compared with AERONET data at 550 nm that were interpolated using bands of 440 or 500 nm (subscript 1) and 675 nm (subscript 2) as:

$$\ln \tau_{550nm} = \ln \tau_1 + \frac{\ln(\tau_2/\tau_1)}{\ln(\lambda_2/\lambda_1)} \qquad (8)$$

[60] In order to make the comparison more meaningful, the modeled AOD is derived by combining modeled carbonaceous and sulfate aerosol data with a climatology of sea salt and mineral dust aerosols provided by N. Mahowald [*Luo et al.*, 2003; *Mahowald et al.*, 2006]. The contribution of the sea salt and mineral dust aerosols to the total modeled AOD varies depending on sites, ranging from 1.1% to 71.4% in EEA run and from 1.4% to 77.3% in ECA run. The comparison between the modeled AOD values and AERONET measurements indicates that the difference between the two is within the factor of two at most sites which is similar to the aerosol mass evaluations as described previously in section 3.2.

4. Direct Radiative Forcing of Carbonaceous and Sulfate Aerosols

[61] Direct Radiative Effect (DRE) of aerosols is defined as the difference between the radiative fluxes derived by

Figure 15. Comparisons of modeled aerosol number concentrations with the NOAA/ESRL observations at multiple stations over the Northern Hemisphere. Cutoff diameter is 10 nm for both model and observations.

including total (natural and anthropogenic) aerosols while Direct Radiative Forcing (DRF) includes only anthropogenic aerosols [e.g., *Yu et al.*, 2006]. Since the sources of the carbonaceous and sulfate aerosols are mainly anthropogenic, the present estimates represent DRF.

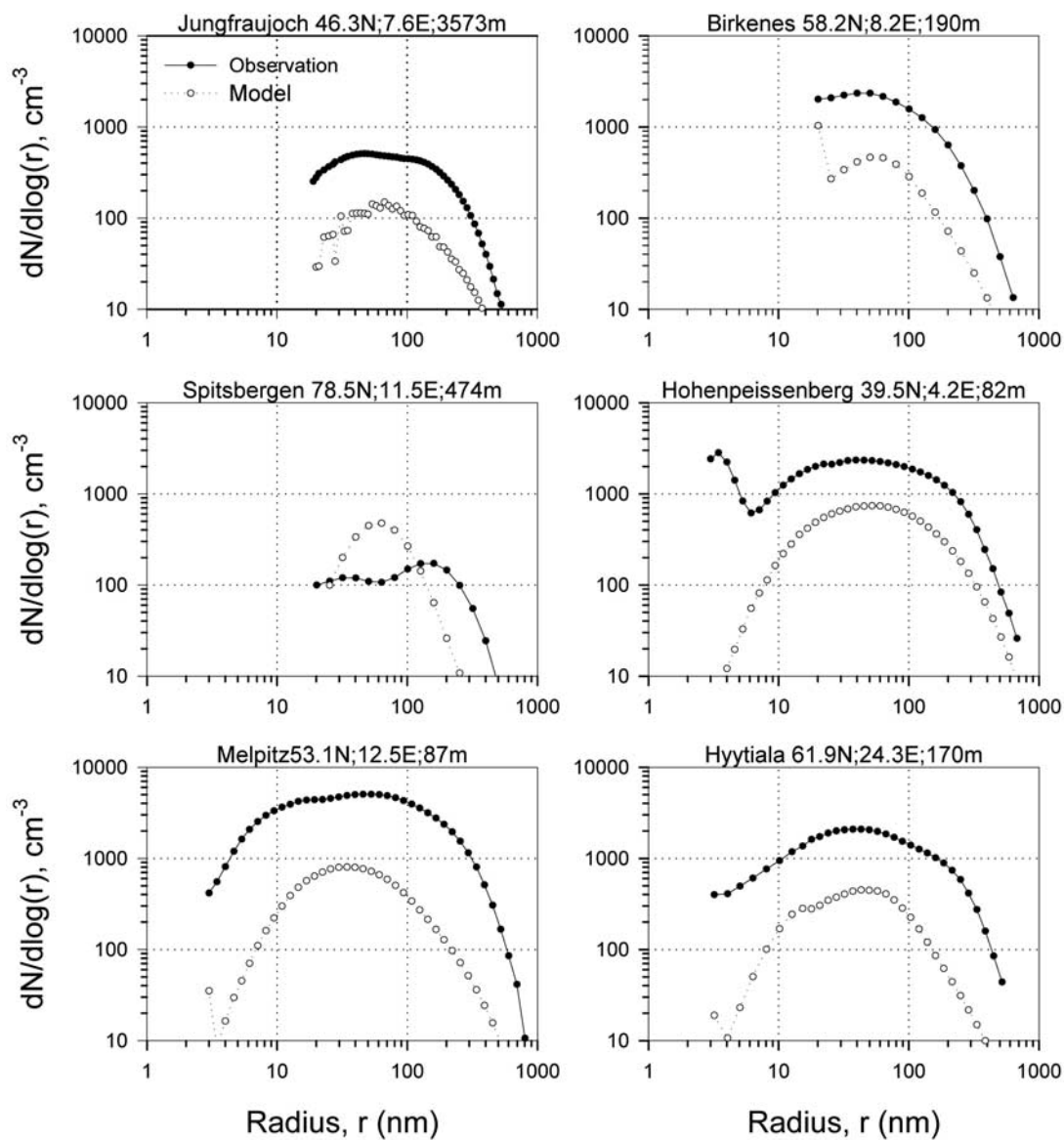### 4.1. Impact of Aerosol Mixing State and Size Distribution on Modeled Direct Radiative Forcing

[62] The geographical distribution of clear-sky and all-sky direct radiative forcing at the TOA by external BC shows small differences among the results calculated using the two different methods (i.e., single moment vs. 2-moment), although the 2-moment scheme does enhance the magnitude of the forcing over regions with high aerosol loading (e.g., East and South Asia). The global average forcing is also higher (Figures 20a to 20d). While the external BC mode generates mostly positive forcing at the top of the atmosphere, the forcing of the mixed aerosol mode MBS (that also contains the light-absorbing black carbon) display both negative and positive values (Figures 20e to 20h).

[63] The sign of aerosol clear-sky radiative forcing at TOA is determined by the critical single scattering albedo (CSSA) that is a function of both surface albedo (R_s; the surface reflectivity) and the upward fraction of scattered radiation (β; an aerosol optical property, see *Ackerman and Toon*, 1981; *Hansen et al.*, 1997; *Seinfeld and Pandis*, 1998). In the all-sky case, the CSSA is governed by the albedo beneath the aerosol layer. When the single scattering albedo of atmospheric aerosols is higher than the CSSA, the TOA aerosol forcing is negative and vice versa. The single scattering albedo of MBS aerosols is always lower than that of pure sulfate aerosols so that the mixed aerosol is a more effective absorber of solar radiation (see Figure 3b). The single scattering albedo of the MBS (0.35 to 0.84 for wavelengths <500 nm) can be higher than CSSA over specific regions with low surface albedo for the clear sky case. Such regions include most of the oceans and certain land areas (e.g., the Mediterranean, eastern United States, part of India, and eastern China; not shown). The TOA forcing of MBS over these regions is primarily negative.

[64] There is a clear difference between the DRF patterns at the TOA between the results of the two aerosol mixing schemes dealing with MBS (Figures 20e to 20h). Specifically, negative clear sky forcing appears over much wider
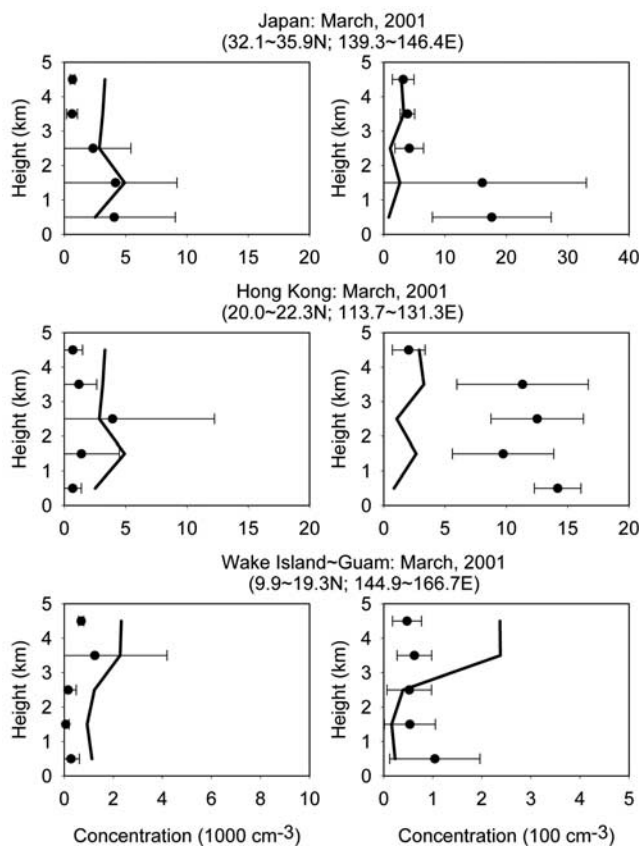
Figure 16. Comparisons between observed and model predicted aerosol size distributions. Measurements are for all aerosols and model predictions include carbonaceous and sulfate aerosols only.

regions using the core-shell method than using the internally mixed method, implying the less significant impact of core-shell than internally mixed structure on the single scattering albedo of mixed BC-containing aerosols [*Ackerman and Toon*, 1981; *Bond et al.*, 2006].

[65] The direct radiative forcing of the external sulfate aerosols at the TOA of all the runs using 2-moment scheme are much smaller (-0.77 W m^{-2} in global mean in ECA and EHA, -0.61 W m^{-2} in ECE; Table 8) compared to the case using single moment aerosol model (-2.03 in EEA and -1.81 W m^{-2} in EEE; Table 8). As expected, the high negative TOA forcing appears over places with high SO$_2$ emissions (Figure 21). This result suggests a critical role of an explicit prediction of the size distribution in determining the total radiative forcing of external sulfate aerosols. On the other hand, the mixed particles in the model would compete with external sulfate aerosols for sulfate mass and thus leads to a reduction of external sulfate forcing. A similar conclusion has also been drawn by *Bauer and Koch* [2005]. Additionally, the coated reflecting material on absorbing aerosols would change the single scattering albedo and also extinction strength of these particles. In combination, these effects due to mixing state of aerosols can further reduce the negative forcing at the TOA as indicated by our study and others [e.g., *Jacobson*, 2001b; *Bond et al.*, 2006; *Stier et al.*, 2006; *Koch et al.*, 2007]. The ~20% difference between the external sulfate TOA forcing of ECA and ECE runs (-0.77 vs. -0.61) implies that the mixing state is a nonnegligible effect even though it is a smaller effect than that attributed to the different size distributions.
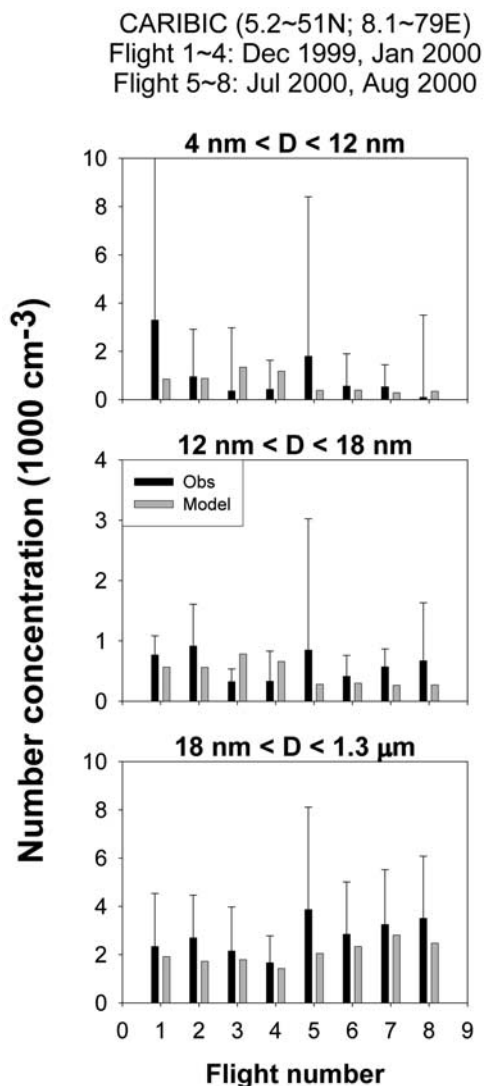
Figure 17. Comparisons between model estimated (line) and TRACE-P measured (dot) aerosol number concentrations. Two size ranges in diameters of observation are $0.007-0.1$ and $0.1-0.75$ μm for the left and right columns, respectively. Observations are averaged at every 1000 m from surface to 5000 m, and the standard deviation is used as the error bar. Three-year mean model results at corresponding layer are used.

[66] When internal mixtures are included in the model, the estimated global mean of clear-sky (all-sky) direct radiative forcing of total carbonaceous and sulfate aerosols with the single-moment and all-external mixture (for radiation calculation) scheme are calculated to be -2.09 (-0.71) W m^{-2} at TOA, -3.59 (-2.30) W m^{-2} at surface, and $+1.49$ $(+1.59)$ W m^{-2} in the atmosphere (defined as TOA forcing$-$surface forcing; Run EEA; Table 8). However, when the 2-moment scheme is applied (ECA simulation), the clear-sky (all-sky) radiative forcing is substantially different, for instance, -0.87 (-0.12) W m^{-2} at the TOA, -2.51 (-1.86) W m^{-2} at the surface, and 1.64 $(+1.74)$ W m^{-2} in the atmosphere obtained by using the core-shell model for MBS, implying a significantly reduced cooling effect of the earth$-$atmosphere system while an enhanced warming in the atmosphere compared to the result of EEA (Table 8). The former effect is mainly caused by the reduced TOA forcing of external sulfate by explicitly predicting the size distribution and the latter is due to the enhanced warming effect of mixed aerosols. Interestingly, we find that the result using the external mixture (radiation only) and single moment model (i.e., EEA run) is quite close to

the range of satellite-based estimates of direct radiative forcing due to anthropogenic aerosols of -1.9 ± 0.3 and -0.8 ± 0.1 W m^{-2} as a global average for clear-sky and all-sky, respectively [*Bellouin et al.*, 2005; *Kaufman et al.*, 2005; *Yu et al.*, 2006]. However, our result derived using the more elaborate 2-moment scheme including mixed aerosols (i.e., ECA simulation), is quite close to the range of $-0.68 \pm$ 0.24 for clear-sky and -0.22 ± 0.16 W m^{-2} for all sky obtained by the cluster of models listed in the IPCC AR4 report [*Forster et al.*, 2007].

[67] When internal mixtures are excluded in the model (i.e., runs ECE and EEE), the total mass of sulfate is reduced while the total BC mass in the atmosphere increases

Figure 18. Comparisons of modeled aerosol number concentrations in upper troposphere ($\sim$10 km) with the CARIBIC observations in three size bins. Both modeled results and observational data were scaled to the standard atmosphere (1013.25 hPa and 273.15 K). CARIBIC data between 8 and 12 km are averaged through the flight path, and three layers around 10 km are averaged for CAM3 and standard deviation is shown as error bars.

Table 5. Comparisons of Modeled Submicron Aerosol Number Concentrations and the Observed Aerosol Number Concentrations[a]

| | | Aerosol Number Concentrations, cm^{-3} STP | | | | | |
| | | SH | | | NH | | |
	Aerosol Size	10%	Median	90%	10%	Median	90%
Minikin	$14 < D < 100$ nm	130	240	400	290	770	9600
	$0.1 < D < 1.0$ μm	6	17	34	16	40	90
This Work	$14 < D < 100$ nm	912	1680	2258	1247	1762	2411
	$0.1 < D < 1.0$ μm	2	7	12	10	41	72

[a]Observation data are adopted from *Minikin et al.* [2003]. Model results are averaged over latitude range of $50-56°$S for SH and $52.5-55.5°$N for NH, respectively, along the given longitude $(0-360°)$. Observations are conducted in height range between 9 and 11 km, and the modeled results at three vertical layers centered at 10 km are chosen in the comparison. Three-year averaged April and October monthly mean model data are used for SH and NH, respectively.

drastically due to the disappearance of the strong sink of BC through nucleation scavenging of MBS. As a result, the clear-sky (all-sky) radiative forcing in ECE run is thus -0.37 $(+0.34)$ W m^{-2} at the TOA, -2.44 (-1.85) W m^{-2} at the surface, and $+2.07$ $(+2.19)$ W m^{-2} in the atmosphere, showing a very strong warming compared to the cases where the mixed aerosols are included.

[68] For absorbing aerosols, a substantial difference in the radiative forcing distribution caused by the inclusion of mixed aerosols can be seen as the TOA, atmospheric, and surface clear-sky forcing of MBS aerosols derived using the core-shell model and the external single-moment BIM only model are compared (Figure 22). Note that the former model uses the total mass of MBS (sulfate plus BC in the mixed mode) while the latter uses only BC mass in the mixed mode (BIM) to calculate the absorption, although the total masses of BC involved in both calculations are actually the same (i.e., BIM). The atmospheric forcing derived using the mixed aerosol model is up to 2 times larger than that derived by the external mixing model in the NH. The narrow dispersion below the 1:1 line in Figures 22c and 22d comes from different total absorbing optical depths (a combined result of mass, single scattering albedo, and size distribution) derived in the two schemes. This enhancement of the atmospheric forcing by the mixed aerosol extends to the surface forcing: the mixed aerosol model produces a surface forcing that doubles the external BIM only model result in the NH and to a less extent in the SH. In comparison, the difference between the TOA forcing derived by the two methods is much smaller in magnitude but often seen with different signs over various geographical locations. Evidently, the enhancement of absorbing aerosol radiative forcing when using the 2-moment scheme compared to the 1-moment scheme is seen much more

clearly in the NH than in SH. This hemispheric difference is due to the much darker surface in the Southern Hemisphere than that in the Northern Hemisphere. When a different 2-moment scheme for the MBS mode is used, the atmospheric forcing of MBS calculated using the well-mixed scheme is found to be about 6% larger than the core-shell model result in both clear-sky and all-sky conditions (not shown).

[69] Generally speaking, the MBS aerosol mode in the current model appears to be a strong agent for both scattering and absorbing solar radiation, leading to a very small forcing at the TOA but a strong heating in the atmosphere. Our results are consistent with theoretical studies based on various core-shell ratio of mixed aerosols [e.g., *Ackerman and Toon*, 1981; *Bond et al.*, 2006] and are also supported by the recent field experiment results such as the Indian Ocean Experiment (INDOEX) [*Ramanathan et al.*, 2001b, 2007].

[70] All the results indicate that the major factors that cause the different estimates of the modeled total radiative forcing of aerosols are whether the model includes the internally mixed aerosols with both absorbing and reflecting constituents and how the optical properties of these aerosols are represented in the radiation calculations. Our study indicates that by simply adding together the effects of reflecting aerosols and absorbing aerosols, derived separately as externally mixed species, the DRF would not be adequately represented.

4.2. Enhancement of Direct Radiative Forcing of Aerosols by Clouds

[71] We find a substantial difference between the TOA all-sky and clear-sky forcing of BC + MBS aerosols. Table 8 shows that the all-sky forcing is 0.34 W m^{-2} higher than

Table 6. Comparisons of Observed Submicron Aerosol Number Concentrations and Model Predicted Aerosol Number Concentrations[a]

Reference	Name	Latitude, °N	Longitude, °E	Altitude, m	Size, nm	Time	Observation, cm^{-3}	Model, cm^{-3}
Yum et al. [2005]	Korea	36	126	50	$D > 10$	May	8313	9465
Gras [1990]	Cape Grim	−41	145	94	$D > 10$	Ann	2500	1908
Harvey et al. [1991]	Ross Island, Antarctica	−78	164	3300	$D > 2.5$	November	960	2740
Gras [1993]	Mawson, Antarctica	−67	63	32	$D > 10$	February	600	2220
Gras [1993]	Mawson, Antarctica	−67	63	32	$D > 10$	July	80	3741
Hudson and Da [1996]	Reno, Nevada	40	−120	1400	$D > 10$	May	2500	2886
Hudson and Da [1996]	Reno, Nevada	40	−120	1400	$D > 10$	September	8000	4182

[a]Lower boundaries for both model and observations are given. Upper boundary for model and most observations are 100 nm. Three-year averaged modeled results of sulfate containing aerosol modes of AIT, ACC, OC, MBS, and MOS in the months corresponding to the measurement durations are selected in the comparison.

Table 7. Global Mean Atmospheric Anthropogenic Aerosol Optical Depths by This Study, AeroCom [*Kinne et al.*, 2006], and GOCART [*Chin et al.*, 2002] Estimates[a]

Aerosol Mode	This Study, 350–640 nm					AeroCom[b], 550 nm	GOCART, 500 nm
	EEA 1-Moment	ECA 2-Moment	EHA 2-Moment	EEE 1-Moment	ECE 2-Moment		
BC	2.74×10^{-3}	3.06×10^{-3}	3.06×10^{-3}	5.31×10^{-3}	5.31×10^{-3}	4×10^{-3}	7×10^{-3}
BIM (MBS)	2.08×10^{-3}	3.95×10^{-3}	3.98×10^{-3}	–	–		
OC	2.05×10^{-3}	3.75×10^{-3}	3.75×10^{-3}	4.65×10^{-3}	3.95×10^{-3}	1.9×10^{-3}	1.7×10^{-2}
OIM (MOS)	2.57×10^{-3}	1.05×10^{-2}	1.05×10^{-2}	–	–		
SO$_4$[c]	5.72×10^{-2}	1.95×10^{-2}	1.95×10^{-2}	5.21×10^{-2}	1.45×10^{-2}	3.4×10^{-2}	4.0×10^{-2}
Total	6.67×10^{-2}	4.09×10^{-2}	4.09×10^{-2}	6.21×10^{-2}	2.38×10^{-2}	4.0×10^{-2}	6.4×10^{-2}

[a]Mean AOD values for the different aerosol mixing states are given for the model.

[b]The represented AeroCom values are the median of the 16 participated models.

[c]SO$_4$ represents the sum of forcing by NUC, AIT, ACC, and MSO4 (sulfate in mixed aerosols) for EEA run; the sum of AIT and ACC is used for ECA and EHA runs; the sum of NUC, AIT, ACC for EEE and ECE runs.

the clear-sky forcing by BC + MBS aerosols. This difference is attributed to the existence of bright low clouds beneath the aerosol layer that increase the solar albedo of many locations that would otherwise have dark surfaces (such as oceans). To further demonstrate this point, we analyze the relationship between the TOA forcing enhancement by the low clouds (defined as all-sky−clear-sky forcing) and the enhancement of albedo by the low clouds (Alb_E) defined as:

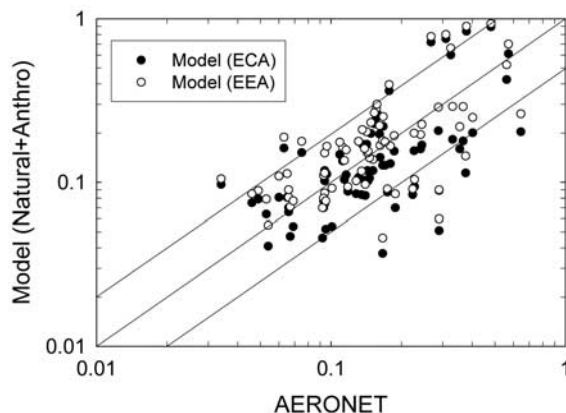$$Alb_E = \frac{(Alb_C - Alb_S) \times f_{cloud}}{Alb_S} \quad (9)$$

where f_{cloud} is the low level cloud fraction, Alb_S is the model estimated surface albedo. A relatively high constant cloud albedo (Alb_C) of 0.8 is applied to emphasize the cloud effect. Here lower Alb_E values indicate that cloud reflection is not very important to the enhancement of all-sky forcing and vice versa. A large number of grid points with significant enhancement of TOA forcing of aerosols in the MBS mode and external BC mode by the low clouds is found in the analysis (Figure 23). Specifically, two distinct regions where the albedo enhancement by the low clouds ranges between $0 \sim 2$ and $2 \sim 6$, corresponding to land and ocean respectively are identified in Figure 23. In both regions, the enhancement of TOA forcing of the absorbing aerosols (MBS and BC) by low clouds increases with the albedo enhancement by clouds, implying the critical role of clouds below the aerosol layer in determining the quantity and sign of radiative forcing of mixed absorbing aerosols. The response of radiative forcing to low cloud enhancement of albedo over the oceans is quite consistent while the response over the land varies drastically, ranging from nearly nonresponding to much larger change with albedo enhancement than that over the oceans. This is because the R_{BM} and thus the single scattering albedo of MBS is generally smaller while the AOD is much higher over the lands than over the oceans (see Figure 7 and related discussions). In most places, MBS is already causing a positive forcing at the TOA.

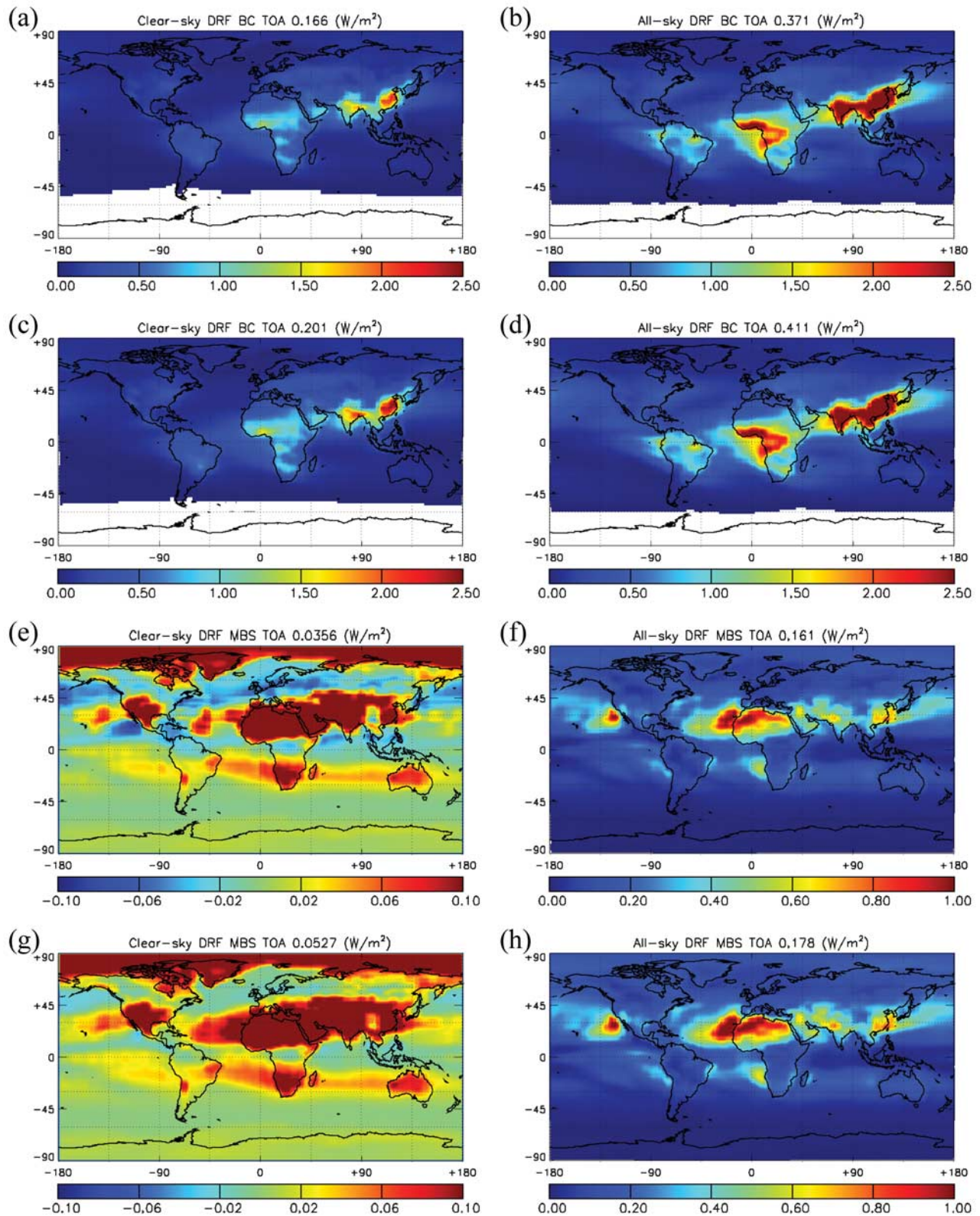## 4.3. Sensitivity of Modeled Results to BC and Primary OC Emissions

[72] The uncertainty in emissions has a potential influence on the modeled results. It is thus important to perform sensitivity tests with different emissions to reveal such an impact. Model results of the BCA and ECA runs that use BC and primary OC emission data from *Bond et al.* [2004]

and from the MIT EPPA model [*Mayer et al.*, 2000; *Wang*, 2004], respectively, are compared in this study. The BC and primary OC emissions of *Bond et al.* [2004] are nearly 44 and 38% lower than those of EPPA, respectively. The most substantial differences (Figure 2) between the two emission data sets are found over India, North Africa, Central Asia, and Eastern US for both BC and primary OC, and in Europe and China for primary OC as well. Note that all other parameters including SO$_2$, DMS, and VOC emissions are identical in these two simulations.

[73] Interestingly, the substantial differences in BC and primary OC emissions do not force a proportional change in the atmospheric aerosol distribution and DRF. Comparing the run using Bond emission inventory (BCA) to the run using EPPA emissions (ECA), the abundance of external BC decreases about 50%, BIM decreases about 31%, OC and OIM decrease about 33% and 14%, respectively (Table 9). The nonproportional change of BIM and OIM,

Figure 19. Comparisons of the annual mean aerosol optical depth (AOD) between model estimates (350–640 nm wave band) and AERONET measurements (550 nm) at 76 sites. In the model estimations, the values of carbonaceous and sulfate aerosols are from the EEA (one-moment) and ECA (two-moment) runs. Natural AOD of climatological sea-salt is adopted from *Mahowald et al.* [2006], and mineral dust is adopted from *Luo et al.* [2003]. Annual means AEROENT AOD are obtained in the period 1999 and 2006. Note that some AERONET sites include missing months.

Figure 20. Modeled clear-sky (left) and all-sky (right) direct radiative forcings of the light absorbing aerosols at TOA. The first and second rows are the forcings of external BC mode calculated using one-moment method (EEA run) and two-moment method (ECA and EHA run), respectively. The third and fourth rows are the results of core-shell mixed MBS (ECA run) and homogeneously mixed MBS (EHA run), respectively.

Table 8. Global Mean Atmospheric Clear-Sky and All-Sky Direct Radiative Forcing (W m^{-2})

	Case	Level	Black Carbons		Sulfate	Organic Carbons		
			BC	BIM[a] (MBS)	SO$_4$[b]	OC	OIM[a] (MOS)	Sum
Clear-Sky Forcing, W m^{-2}	EEA	TOA	0.166	0.090	−2.025	−0.181	−0.142	−2.092
		Surf	−0.760	−0.346	−2.029	−0.252	−0.199	−3.586
		Atmos	0.926	0.436	0.004	0.071	0.057	1.494
	ECA	TOA	0.202	0.036	−0.773	−0.110	−0.222	−0.867
		Surf	−0.779	−0.457	−0.780	−0.159	−0.331	−2.506
		Atmos	0.981	0.493	0.008	0.049	0.109	1.640
	EHA	TOA	0.202	0.053	−0.773	−0.110	−0.222	−0.850
		Surf	−0.779	−0.469	−0.780	−0.159	−0.331	−2.518
		Atmos	0.981	0.522	0.008	0.049	0.109	1.669
	EEE[c]	TOA	0.344	–	−1.809	−0.402	–	−1.867
		Surf	−1.497	–	−1.812	−0.564	–	−3.873
		Atmos	1.841	–	0.003	0.162	–	2.006
	ECE[c]	TOA	0.414	–	−0.613	−0.168	–	−0.367
		Surf	−1.534	–	−0.632	−0.271	–	−2.437
		Atmos	1.948	–	0.020	0.102	–	2.070
All-Sky Forcing, W m^{-2}	EEA	TOA	0.372	0.194	−1.103	−0.097	−0.079	−0.714
		Surf	−0.601	−0.280	−1.106	−0.172	−0.141	−2.300
		Atmos	0.973	0.473	0.002	0.076	0.062	1.586
	ECA	TOA	0.411	0.162	−0.499	−0.062	−0.129	−0.117
		Surf	−0.620	−0.375	−0.506	−0.114	−0.247	−1.861
		Atmos	1.031	0.536	0.006	0.052	0.118	1.744
	EHA	TOA	0.411	0.178	−0.499	−0.062	−0.129	−0.101
		Surf	−0.620	−0.389	−0.506	−0.114	−0.247	−1.875
		Atmos	1.031	0.567	0.006	0.052	0.118	1.775
	EEE[c]	TOA	0.757	–	−0.957	−0.220	–	−0.420
		Surf	−1.195	–	−0.958	−0.394	–	−2.547
		Atmos	1.952	–	0.001	0.174	–	2.127
	ECE[c]	TOA	0.835	–	−0.405	−0.092	–	0.339
		Surf	−1.231	–	−0.420	−0.201	–	−1.853
		Atmos	2.067	–	0.015	0.109	–	2.192

[a]BIM (OIM) represents the forcing by BC (OC) in MBS (MOS) for EEA run; MBS (MOS) is used for ECA and EHA runs.

[b]SO$_4$ represents the sum of forcing by AIT, ACC, and MSO4 (sulfate in mixed aerosols) for EEA run; the sum of AIT and ACC is used for ECA and EHA runs.

[c]There are no mixed aerosols in EEE and ECE runs, and the aerosols in the list are externally mixed.

i.e., BC and OC in mixed modes, to the reduction of BC and primary OC emission is a result of the aging scheme in our model that is constrained by not only aging time but also the availability of gaseous sulfuric acid. When emissions of BC and OC are lowered, under the same availability of sulfuric acid relatively more external carbonaceous aerosols could become aged and thus the relative decreases in MBS and MOS with emissions are smaller than those of external ones.

[74] Even though the same emissions of SO$_2$ and DMS are used in both runs, the total mass of external sulfate aerosol modes (NUC, AIT, and ACC) in the BCA run increase 16, 20, and 8% compared to the ECA run, respectively, and sulfate mass in mixed modes decrease about 13%, all implying a decrease of aerosol surfaces for condensation and coagulation with the reduced BC and OC emissions.
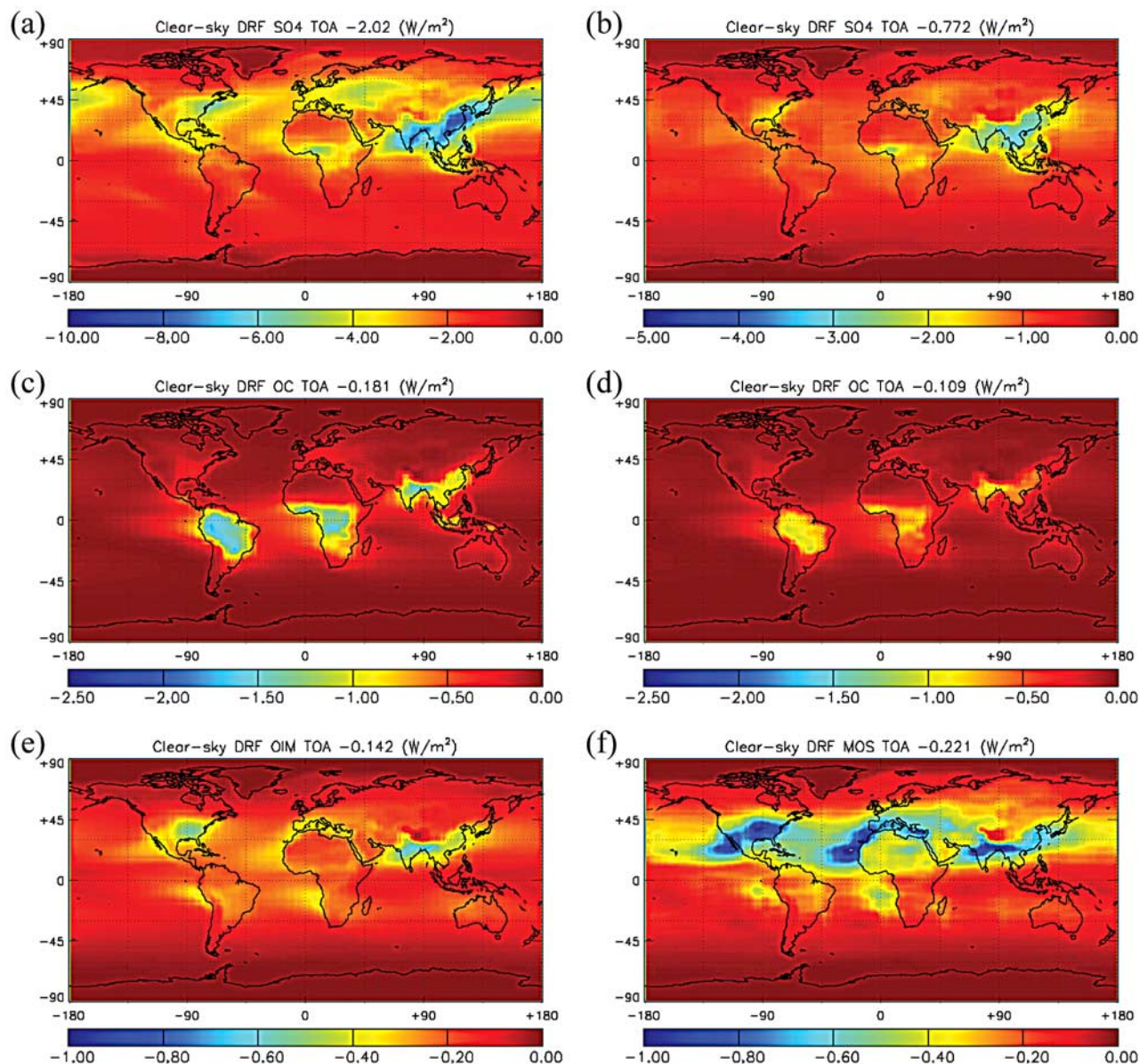
[75] Reduction in BC and primary OC emissions brings in a substantial change in aerosol radiative forcing. As shown in Table 10, decreased BC emissions in the BCA run leads to a reduction of 57% and 50%, respectively in the global mean clear-sky atmospheric forcing of external BC and mixed MBS modes compared to the ECA run. The weakening of OC clear-sky TOA forcing due to the lowered OC emissions is slightly less than for the BC case. However, it still accounts for a 30% and 11% reduction for external OC and MOS, respectively. The relative changes due to the reduction of BC and primary OC emissions of all BC and OC modes are nearly the same for clear-sky and all-sky. The change in BC and OC modes radiative forcing compensate each other to a certain extent due to their opposite sign. This leads to only a small change of 16% in the total clear-sky forcing of the entire carbonaceous and sulfate aerosol family. In contrast, the resulting relative change in the all-sky total TOA radiative forcing of the whole carbonaceous and sulfate aerosols family is very large (almost 2.5 time increase).

[76] The absorbing aerosols (external BC and mixed MBS modes) are much more important to TOA radiative forcing for all-sky than clear-sky as seen in the ECA run results, where the strong positive forcing of absorbing aerosols at the TOA is largely balanced with the negative forcing from all other aerosols. In the BCA run, the reduction of BC causes a 0.23 W m^{-2} weaker positive forcing of absorbing aerosols, nearly 70% of the total TOA forcing of all aerosols in the BCA run. This result demonstrates the strong dependency of modeled radiative forcing of aerosols on the emissions inventory particularly where absorbing aerosols are considered. It is expected that with the Bond emissions of primary carbonaceous aerosols, the global mean TOA all-sky forcing should be kept negative even if the internal mixtures were excluded in the model.
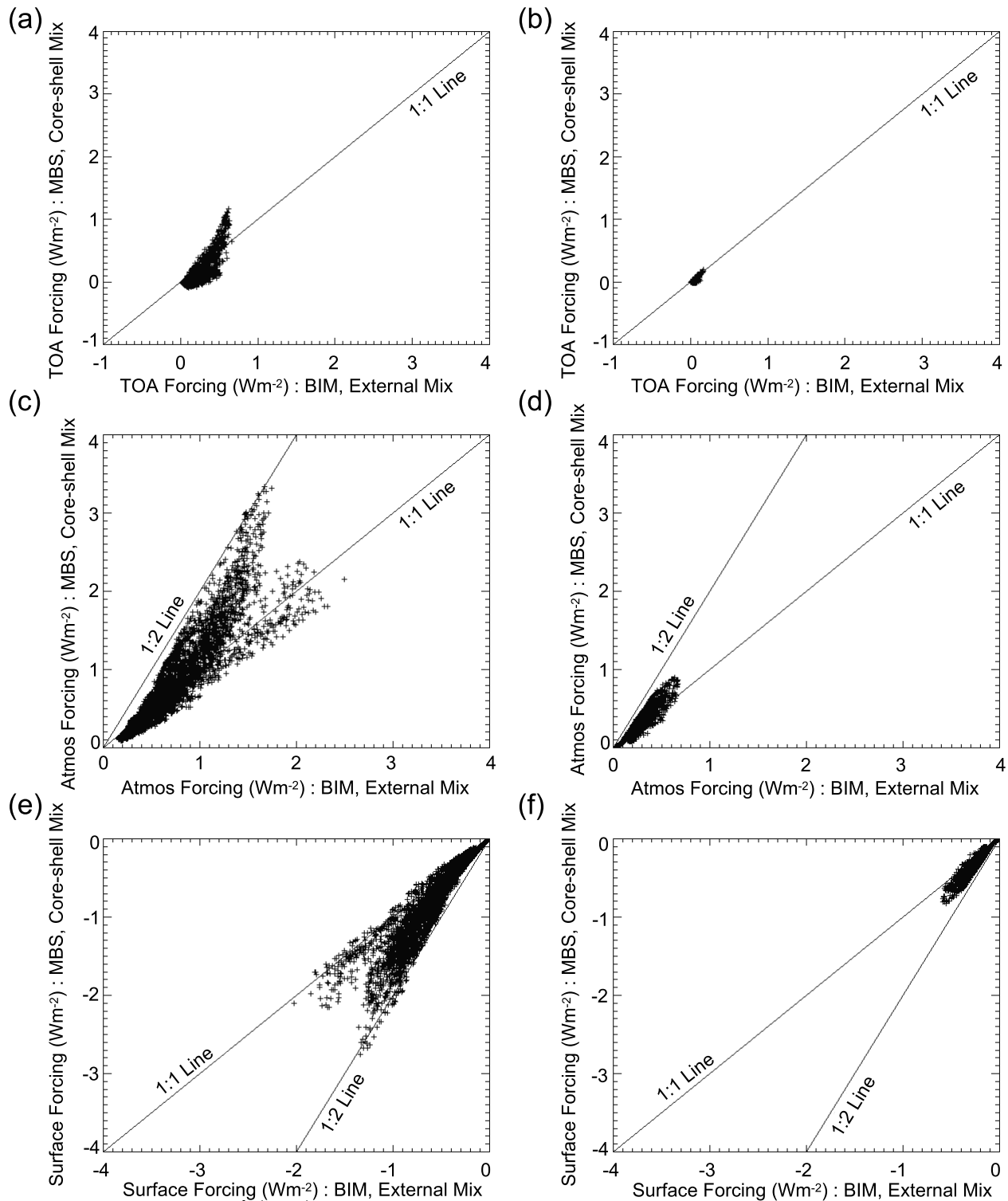
5. Conclusions

[77] A multimode two-moment model of carbonaceous and sulfate aerosols has been developed and coupled to the

Figure 21. Modeled clear-sky direct radiative forcings of sulfate and organic carbon aerosols. Panels in the left column are from the EEA run (one-moment method; OC is assumed to be all externally mixed), and panels in the right column are from the EHA run (two-moment method; external OC and homogeneously mixed MOS).

NCAR CAM3 model. The aerosol model is composed of five external aerosol modes of black carbon, organic carbon, and three types of sulfate aerosols separated by size (nucleation, Aitken, and accumulation modes), and two mixed aerosol modes consisting of BC and sulfate as well as OC and sulfate, respectively. This unique design is consistent with known aerosol production and mixing mechanisms. Aerosol chemical and physical processes such as nucleation, coagulation, condensation, and scavenging along with their radiative effects are formulated based on the size distribution and the chemical properties of the aerosols, including the mixing state.

[78] Modeled aerosol mass and number concentration, size distribution, and optical depth have been compared with a collection of surface and aircraft observations as well as estimates obtained by other model studies. Modeled aerosol mass concentrations are found to be in a reasonable agreement with surface observations at many locations as well as with measured vertical profiles from ACE-Asia and PEM field experiments. The predicted number concentration of particles particularly in accumulation modes is found to agree well with the TRACE-P and CARIBIC measurements. Modeled and observed aerosol size distributions have similar distribution spectra and modes, but the modeled number concentration is lower than the observations,
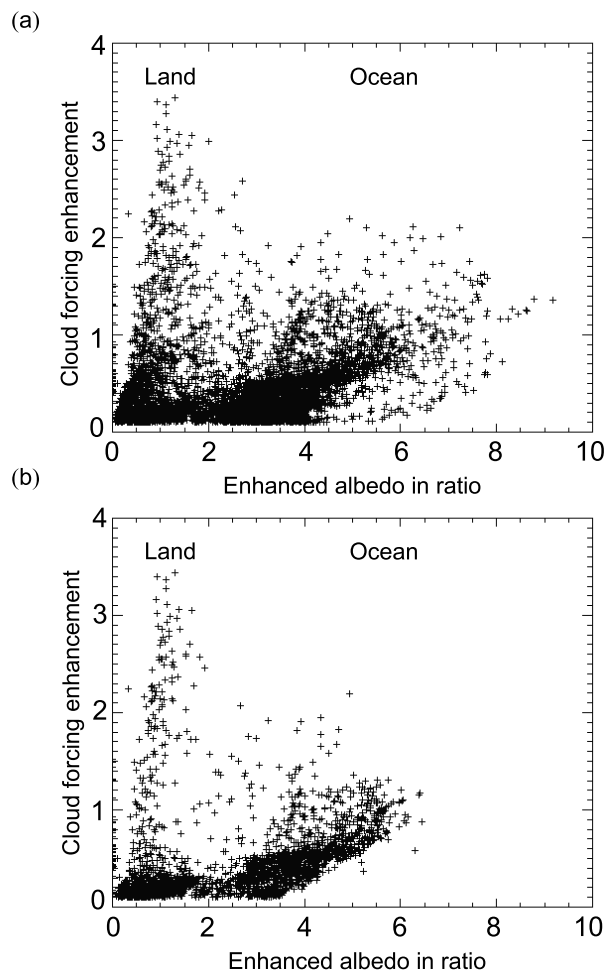
Figure 22. Comparisons of direct radiative forcing by BC-sulfate mixed aerosols between external mix (horizontal axis) and core-shell mix methods (vertical axis): at the TOA (top), in the atmosphere (middle), and at the Earth's surface (bottom). Northern Hemispheric data are shown in the left column, and Southern Hemispheric data are shown in the right column. All data are 3-year means.

most likely due to the lack of natural aerosols in the model and the coarse model resolution.

[79] We have designed several sensitivity simulations with various configurations of mixing state (including or excluding internal mixtures in the model) and different schemes to describe the aerosol size distribution (1-moment or 2-moment, either only in radiation calculation or through out all modeled processes). Comparing to the widely used

Figure 23. Distributions of the cloud forcing enhancement of mixed and external BC aerosol TOA forcing ($F_{\text{all-sky}} - F_{\text{clear-sky}}$) to the enhanced albedo by lower level cloud: (a) global and (b) Northern Hemisphere ($20-70°\text{N}$). The enhanced albedo is the ratio of lower level atmosphere albedo with lower cloud (albedo = 0.8) to the surface albedo. Enhanced albedo is equal to 0 when there is no cloud and is equal to 1 when it is twice larger than surface albedo.

mass-only method with prescribed geometric size of particles (1-moment scheme), the use of prognostic size distributions of aerosols based on a 2-moment scheme in our model leads to a significant reduction in optical depth and thus the radiative forcing at the top of the atmosphere (TOA) of particularly external sulfate aerosols. The inclusion of mixed aerosols alters the mass partitioning of carbonaceous and sulfate aerosol constituents. Specifically, about 35.5%, 48.5%, and 32.2% of BC, OC, and sulfate mass are found in the mixed aerosols. Inclusion of mixed aerosols in the model also brings in competing effects in aerosol radiative forcing. These include a reduction in atmospheric abundance of BC and OC due to the shorter lifetime of internal mixtures (cooling), a mass loss of external sulfate to mixtures (warming), and an enhancement in atmospheric heating per BC mass due to the stronger

absorption extinction of the MBS than external BC (warming). The combined result of including a prognostic size distribution and the mixed aerosols in the model is a much smaller total negative TOA forcing (-0.12 W m^{-2}) of all carbonaceous and sulfate aerosol compounds compared to the cases using 1-moment scheme either excluding or including internal mixtures (-0.42 and -0.71 W m^{-2}, respectively). The results suggest that besides the emission strength, the major factors to cause different estimates of the total radiative forcing of carbonaceous and sulfate aerosols are 1) whether the model includes prognostic size distribution and uses this distribution in radiation calculation; and 2) whether the model includes internally mixed aerosols with both absorbing and reflecting constituents and uses the mixing state in radiation calculation. Our study demonstrates that simply adding together separately derived radiative effects of externally mixed reflecting and absorbing aerosols does not adequately represent the role of mixed aerosols.

[80] The existence of clouds beneath the aerosol layers is critical when determining the sign of the all-sky TOA radiative forcing (the forcing including cloud effects). This is in particular true for radiative effects due to mixed aerosols containing BC. We find that low clouds can lead to a considerably larger positive all-sky forcing due to MBS aerosols at the TOA.

[81] A reduction of BC and primary OC emissions leads to a decrease in the atmospheric abundance of carbonaceous aerosols, although such a decrease is not necessarily proportional to the change in emissions. Nonlinear effects, such as the limitation of sulfuric acid, affect the carbonaceous aerosol aging and thereby the total carbonaceous aerosol mass. The decrease in atmospheric abundance of total carbonaceous aerosols changes the total TOA radiative forcing due to all aerosols. The magnitude of this change is relatively small (16%) for the clear-sky case, but is substantial for the all-sky case (247%) owing to the low absolute value of total aerosol all-sky TOA forcing. The results suggest the BC and primary OC emissions can play an important role in determining the net all-sky direct radiative forcing at TOA.

[82] The aerosol model applied in this study clearly involves uncertainties regarding the parameterizations and various assumptions, including the methods used to calculate the nucleation scavenging, the aging process of carbonaceous aerosols and the release of aqueous sulfate to the air through evaporation of raindrops. Natural aerosol emissions of e.g. mineral dust and sea salt are also not included in the present model study. Further studies to improve these

Table 9. Aerosol Burden From BCA Run and Differences to ECA Run

Aerosol Mode	BCA, Tg or TgS	BCA−ECA, Tg or TgS	Relative Difference[a], %
BC	0.0677	−0.081	−54.5
BIM	0.0570	−0.025	−30.6
MSO4[b]	0.2249	−0.034	−13.2
ACC	0.5832	0.042	7.7
AIT	1.21×10^{-3}	1.99×10^{-4}	19.7
NUC	1.29×10^{-5}	1.79×10^{-6}	16.0
OC	0.5134	−0.256	−33.2
OIM	0.6266	−0.098	−13.5

[a]Relative difference is defined as (BCA − ECA) / ECA × 100 (%).
[b]MSO$_4$ represents the mass of sulfate in MBS and MOS.

Table 10. Clear-Sky and All-Sky Direct Radiative Forcing From BCA Run and Differences to ECA Run

Level	Aerosol Mode	BCA, W m^{-2} Clear-Sky	All-Sky	BCA-ECA, W m^{-2} Clear-Sky	All-Sky	Relative Difference[a], % Clear-Sky	All-Sky
TOA	BC	0.086	0.182	−0.116	−0.229	−57.4	−55.7
	MBS	0.018	0.111	−0.018	−0.051	−50.0	−31.5
	SO$_4$[b]	−0.836	−0.542	−0.063	−0.043	8.2	8.6
	OC	−0.077	−0.043	0.033	0.019	−30.0	−30.6
	MOS	−0.197	−0.114	0.025	0.015	−11.3	−11.6
	Total[c]	−1.005	−0.406	−0.138	−0.289	15.9	247.0
Surface	BC	−0.362	−0.289	0.417	0.331	−53.5	−53.4
	MBS	−0.330	−0.269	0.127	0.106	−27.8	−28.3
	SO$_4$[b]	−0.843	−0.549	−0.063	−0.043	8.1	8.5
	OC	−0.111	−0.079	0.048	0.035	−30.2	−30.7
	MOS	−0.292	−0.217	0.039	0.030	−11.8	−12.1
	Total[c]	−1.938	−1.403	0.568	0.458	−22.7	−24.6
Atmos	BC	0.448	0.471	−0.533	−0.560	−54.3	−54.3
	MBS	0.348	0.381	−0.145	−0.155	−29.4	−28.9
	SO$_4$[b]	0.008	0.006	0.000	0.000	0.0	0.0
	OC	0.034	0.036	−0.015	−0.016	−30.6	−30.8
	MOS	0.095	0.103	−0.014	−0.015	−12.8	−12.7
	Total[c]	0.934	0.997	−0.706	−0.747	−43.0	−42.8

[a]Relative difference is defined as (BCA − ECA) / ECA × 100 (%).
[b]SO$_4$ represents the sum of forcing by AIT and ACC.
[c]Sum of radiative forcing by all aerosol compounds.

schemes, especially using available observations as constraints, are suggested.

References

Abdul-Razzak, H., and S. J. Ghan (2000), A parameterization of aerosol activation: 2. Multiple aerosol types, *J. Geophys. Res.*, *105*(D5), 6837–6844.

Abdul-Razzak, H., S. J. Ghan, and C. Rivera-Carpio (1998), A parameterization of aerosol activation: 1. Single aerosol type, *J. Geophys. Res.*, *103*(D6), 6123–6131.

Ackerman, A. S., and O. S. Toon (1981), Absorption of visible radiation in atmospheric containing mixtures of absorbing and non absorbent particles, *Appl. Opt.*, *20*, 3661–3668.

Adams, P. J., and J. H. Seinfeld (2002), Predicting global aerosol size distributions in general circulation models, *J. Geophys. Res.*, *107*(D19), 4370, doi:10.1029/2001JD001010.

Andreae, M. O., and A. Gelencsér (2006), Black carbon or brown carbon? The nature of light-absorbing carbonaceous aerosols, *Atmos. Chem. Phys. Discuss.*, *6*, 3419–3463.

Babiker, M., et al. (2001), The MIT Emissions Prediction and Policy Analysis (EPPA) Model: Revisions, sensitivities, and comparison of results, *Rep. 71*, MIT Joint Program on the Science and Policy of Global Change, Cambridge, Mass. (Available at http://web.mit.edu/globalchange/www/MITJPSPGC_Rpt71.pdf)

Bahreini, R., J. L. Jimenez, J. Wang, R. C. Flagan, J. H. Seinfeld, J. T. Jayne, and D. R. Worsnop (2003), Aircraft-based aerosol size and composition measurements during ACE-Asia using an Aerodyne aerosol mass spectrometer, *J. Geophys. Res.*, *108*(D23), 8645, doi:10.1029/2002JD003226.

Barth, M. C., P. J. Rasch, J. T. Kiehl, C. M. Benkovitz, and S. E. Schwartz (2000), Sulfur chemistry in the National Center for Atmospheric Research Community Climate Model: Description, evaluation, features, and sensitivity to aqueous chemistry, *J. Geophys. Res.*, *105*(D1), 1387–1416.

Bauer, S. E., and D. Koch (2005), Impact of heterogeneous sulfate formation at mineral dust surfaces on aerosol loads and radiative forcing in the Goddard Institute for Space Studies general circulation model, *J. Geophys. Res.*, *110*, D17202, doi:10.1029/2005JD005870.

Bellouin, N., O. Boucher, J. Haywood, and M. S. Reddy (2005), Global estimate of aerosol direct radiative forcing from satellite measurements, *Nature*, *438*, 1138–1141.

Berner, A., S. Sidla, Z. Galambos, C. Kruisz, R. Hitzenberger, H. ten Brink, and G. Kos (1996), Modal character of atmospheric black carbon size distributions, *J. Geophys. Res.*, *101*(D14), 19,559–19,565.

Binkowski, F. S., and U. Shankar (1995), The Regional Particulate Matter Model: 1. Model description and preliminary results, *J. Geophys. Res.*, *100*(D12), 26,191–26,209.

Bodhaine, B. A. (1995), Aerosol absorption measurements at Barrow, Mauna Loa and the south pole, *J. Geophys. Res.*, *100*(D5), 8967–8975.

Bohren, C. F., and D. R. Huffman (1983), *Absorption and Scattering of Light by Small Particles*, John Wiley, New York.

Bond, T. C., D. G. Streets, K. F. Yarber, S. M. Nelson, J.-H. Woo, and Z. Klimont (2004), A technology-based global inventory of black and organic carbon emissions from combustion, *J. Geophys. Res.*, *109*, D14203, doi:10.1029/2003JD003697.

Bond, T. C., G. Habib, and R. W. Bergstrom (2006), Limitations in the enhancement of visible light absorption due to mixing state, *J. Geophys. Res.*, *111*, D20211, doi:10.1029/2006JD007315.

Briegleb, B. P. (1992), Delta-Eddington approximation for solar radiation in the NCAR Community Climate Model, *J. Geophys. Res.*, *97*(D7), 7603–7612.

Cantrell, B. K., and K. T. Whitby (1978), Aerosol size distributions and aerosol volume formation for a coal-fired power-plant plume, *Atmos. Environ.*, *12*, 323–333.

Chin, M., P. Ginoux, S. Kinne, O. Torres, B. N. Holben, B. N. Duncan, R. V. Martin, J. A. Logan, A. Higurashi, and T. Nakajima (2002), Tropospheric aerosol optical thickness from the GOCART model and comparisons with satellite and Sun photometer measurements, *J. Atmos. Sci.*, *59*, 461–483.

Chung, S. H., and J. H. Seinfeld (2002), Global distribution and climate forcing of carbonaceous aerosols, *J. Geophys. Res.*, *107*(D19), 4407, doi:10.1029/2001JD001397.

Chylek, P., and J. Hallett (1992), Enhanced absorption of solar radiation by cloud droplets containing soot particles in their surface, *Q. J. R. Meteorol. Soc.*, *118*, 167–172.

Chylek, P., G. Videen, D. Ngo, R. G. Pinnick, and J. D. Klett (1995), Effect of black carbon on the optical properties and climate forcing of sulfate aerosols, *J. Geophys. Res.*, *100*(D8), 16,325–16,332.

Clarke, A. D., et al. (2004), Size distributions and mixtures of dust and black carbon aerosol in Asian outflow: Physiochemistry and optical properties, *J. Geophys. Res.*, *109*, D15S09, doi:10.1029/2003JD004378.

Collins, W., et al. (2006), The community climate system model: CCSM3, *J. Clim.*, *19*, 2122–2143.

Cooke, W. F., and J. J. N. Wilson (1996), A global black carbon aerosol model, *J. Geophys. Res.*, *101*(D14), 19,395–19,410.

Cooke, W. F., C. Liousse, H. Cachier, and J. Feichter (1999), Construction of a 1° × 1° fossil fuel emission data set for carbonaceous aerosol and implementation and radiative impact in the ECHAM4 model, *J. Geophys. Res.*, *104*(D18), 22,137–22,162.

Cooke, W. F., V. Ramaswamy, and P. Kasibhatla (2002), A general circulation model study of the global carbonaceous aerosol distribution, *J. Geophys. Res.*, *107*(D16), 4279, doi:10.1029/2001JD001274.

d'Almeida, G. A., P. Koepke, and E. P. Shettle (1991), *Atmospheric Aerosols: Global Climatology and Radiative Characteristics*, A. Deepak, Hampton, Va.

Dusek, U., D. S. Covert, A. Wiedensohler, C. Neusüss, and D. Weise (2004), Aerosol number to volume ratios in Southwest Portugal during ACE-2, *Tellus*, *56B*, 477–491.

Ekman, A. M. L., C. Wang, J. Wilson, and J. Strom (2004), Explicit simulation of aerosol physics in a cloud-resolving model: A sensitivity study based on an observed convective cloud, *Atmos. Chem. Phys.*, *4*, 773–791.

Ekman, A. M. L., C. Wang, J. Strom, and R. Krejci (2006), Explicit simulation of aerosol physics in a cloud-resolving model: Aerosol transport and processing in the free troposphere, *J. Atmos. Sci.*, *63*, 682–696.

Ekman, A. M. L., A. Engstrom, and C. Wang (2007), The effect of aerosol composition and concentration on the development and anvil properties of a continental deep convective cloud, *Quart. J. Roy. Meteor. Soc.*, *133*, 1439–1452.

Feingold, G., and S. Kreidenweis (2000), Does cloud processing of aerosol enhance droplet concentrations?, *J. Geophys. Res.*, *105*(D19), 24,351–24,361.

Forster, P., et al. (2007), Changes in atmospheric constituents and in radiative forcing, in *Climate Change, 2007. The Physical Science Basis. Contribution of Working Group I to the Fourth Assessment Report of the Intergovernmental Panel on Climate Change*, edited by S. Solomon et al., Cambridge Univ. Press, Cambridge, U.K.

Fuller, K. A., W. C. Malm, and S. M. Kreidenweis (1999), Effect of mixing on extinction by carbonaceous particles, *J. Geophys. Res.*, *104*(D13), 15,941–15,954.

Ghan, S. J., and S. E. Schwartz (2007), Aerosol properties and processes: A path from field and laboratory measurements to global climate models, *Bull. Amer. Meteorol. Soc.*, *88*, 1059–1083.

Gras, J. L. (1990), Baseline atmospheric condensation nuclei at Cape Grim, 1977–1987, *J. Atmos. Chem.*, *11*, 89–106.

Gras, J. L. (1993), Condensation nucleus size distribution at Mawson, Antarctica: Seasonal cycle, *Atmos. Environ., Part A*, *27*, 1417–1425.

Griffin, R. J., D. Dabdub, D. Cocker III, and J. H. Seinfeld (1999), Estimate of global atmospheric organic aerosol from oxidation of biogenic hydrocarbons, *Geophys. Res. Lett.*, *26*(17), 2721–2724.

Hack, J. J., J. M. Caron, S. G. Yeager, K. W. Oleson, M. M. Holland, J. E. Truesdale, and P. J. Rasch (2006), Simulation of the global hydrological cycle in the CCSM Community Atmosphere Model (CAM3): Mean features, *J. Clim.*, *19*, 2199–2221.

Hansen, J., M. Sato, and R. Ruedy (1997), Radiative forcing and climate response, *J. Geophys. Res.*, *102*(D6), 6831–6864.

Hara, K., S. Yamagata, T. Yamanouchi, K. Sato, A. Herber, Y. Iwasaka, M. Nagatani, and H. Nakata (2003), Mixing states of individual aerosol particles in spring Arctic troposphere during ASTAR 2000 campaign, *J. Geophys. Res.*, *108*(D7), 4209, doi:10.1029/2002JD002513.

Harrington, D. Y., and S. M. Kreidenweis (1998), Simulation of sulfate aerosol dynamics: I. Model Description, *Atmos. Environ.*, *32*, 1691–1700.

Harvey, M. J., G. W. Fisher, I. S. Lechner, P. Issac, N. E. Flower, and A. L. Dick (1991), Summertime aerosol measurements in the Ross Sea region of Antarctica, *Atmos. Environ., Part A*, *25*, 569–580.

Hasegawa, S., and S. Ohta (2002), Some measurements of the mixing state of soot-containing particles at urban and nonurban sites, *Atmos. Environ.*, *36*, 3899–3908.

Haywood, J. M., and K. P. Shine (1995), The effect of anthropogenic sulfate and soot aerosol on the clear sky planetary radiation budget, *Geophys. Res. Lett.*, *22*(5), 603–606.

Heintzenberg, J., M. Hermann, and D. Theiss (2003), Out of Africa: High aerosol concentrations in the upper troposphere over Africa, *Atmos. Chem. Phys.*, *3*, 1191–1198.

Hermann, M., J. Heintzenberg, A. Wiedensohler, A. Zahn, G. Heinrich, and C. A. M. Brenninkmeijer (2003), Meridional distributions of aerosol particle number concentrations in the upper troposphere and lower stratosphere obtained by Civil Aircraft for Regular Investigation of the Atmosphere Based on an Instrument Container (CARIBIC) flights, *J. Geophys. Res.*, *108*(D3), 4114, doi:10.1029/2001JD001077.

Hess, M., P. Koepke, and I. Schult (1998), Optical properties of aerosols and clouds: The software package OPAC, *Bull. Am. Met. Soc.*, *79*, 831–844.

Hoppel, W. A., G. M. Frick, J. W. Fitzgerald, and R. E. Larson (1994), Marine boundary layer measurements of new particle formation and the effects nonprecipitating clouds have on aerosol size distribution, *J. Geophys. Res.*, *99*(D7), 14,443–14,459.

Hudson, J. G., and X. Da (1996), Volatility and size of cloud condensation nuclei, *J. Geophys. Res.*, *101*(D2), 4435–4442.

Jacobson, M. Z. (2000), A physically-based treatment of elemental carbon optics: Implication for global direct forcing of aerosols, *Geophys. Res. Lett.*, *27*(2), 217–220.

Jacobson, M. Z. (2001a), Global direct radiative forcing due to multicomponent anthropogenic and natural aerosols, *J. Geophys. Res.*, *106*(D2), 1551–1568.

Jacobson, M. Z. (2001b), Strong radiative heating due to the mixing state of black carbon in atmospheric aerosols, *Nature*, *409*, 695–697.

Jensen, E. J., O. B. Toon, H. B. Selkirk, J. D. Spinhirne, and M. R. Schoeberl (1996), On the formation and persistence of subvisible cirrus clouds near the tropical torpopause, *J. Geophys. Res.*, *101*(D16), 21,361–21,375.

John, W., S. M. Wall, J. L. Ondo, and W. Winklmyr (1990), Modes in the size distribution of atmospheric inorganic aerosol, *Atmos. Environ., Part A*, *24*, 2349–2359.

Kanakidou, M., et al. (2005), Organic aerosol and global climate modelling: A review, *Atmos. Chem. Phys.*, *5*, 1053–1123.

Kaufman, Y. J., and R. S. Fraser (1997), The effect of smoke particles on cloud and climate forcing, *Science*, *277*, 1636–1639.

Kaufman, Y. J., O. Boucher, D. Tanre, M. Chin, L. A. Remer, and T. Takemura (2005), Aerosol anthropogenic component estimated from satellite data, *Geophys. Res. Lett.*, *32*, L17804, doi:10.1029/2005GL023125.

Kettle, A. J., M. O. Andreae, D. Amouroux, and T. W. Andreae (1999), A global database of sea surface dimethylsulfide (DMS) measurements and a procedure to predict sea surface DMS as a function of latitude, longitude, and month, *Global Biogeochem. Cycles*, *13*(2), 399–444.

Kiehl, J. T., and B. P. Briegleb (1993), The relative roles of sulfate aerosols and greenhouse gases in climate forcing, *Science*, *260*, 311–314.

Kiehl, J. T., T. L. Schneider, P. J. Rasch, M. C. Barth, and J. Wong (2000), Radiative forcing due to sulfate aerosols from simulations with the National Center for Atmospheric Research Community Climate Model, Version 3, *J. Geophys. Res.*, *105*(D1), 1441–1457.

Kinne, S., et al. (2006), An AeroCom initial assessment - optical properties in aerosol component modules of global models, *Atmos. Chem. Phys.*, *6*, 1815–1834.

Koch, D., D. Jacob, I. Tegen, D. Rind, and M. Chin (1999), Tropospheric sulfur simulation and sulfate direct radiative forcing in the Goddard Institute for Space Studies general circulation model, *J. Geophys. Res.*, *104*(D19), 23,799–23,822.

Koch, D., T. C. Bond, D. Streets, and N. Unger (2007), Linking future aerosol radiative forcing to shifts in source activities, *Geophys. Res. Lett.*, *34*, L05821, doi:10.1029/2006GL028360.

Koepke, P., M. Hess, I. Schult, and E. Shettle (1997), Global Aerosol Data Set, *Rep. 243*, Max Planck Institute for Meteorology, Hamburg.

Kulmala, M., L. Pirjola, and J. M. Mäkelä (2000), Stable sulphate clusters as a source of new atmospheric particles, *Nature*, *404*, 66–69.

Kulmala, M., et al. (2004), Formation and growth rates of ultrafine atmospheric particles: A review of observations, *J. Aerosol Sci.*, *35*, 143–176.

Lammel, G., and T. Novakov (1995), Water nucleation properties of carbon black and diesel soot particles, *Atmos. Environ.*, *29*, 813–823.

Lee, S.-H., J. M. Reeves, J. C. Wilson, D. E. Hunton, A. A. Viggiano, T. M. Miller, J. O. Ballenthin, and L. R. Lait (2003), Particle formation by ion nucleation in the upper troposphere and lower stratosphere, *Science*, *301*, 1886–1889.

Liousse, C., J. E. Penner, C. Chuang, J. J. Walton, H. Eddleman, and H. Cachier (1996), A global three-dimensional model study of carbonaceous aerosols, *J. Geophys. Res.*, *101*(D14), 19,411–19,432.

Liu, X., J. E. Penner, and M. Herzog (2005), Global modeling of aerosol dynamics: Model description, evaluation, and interactions between sulfate and nonsulfate aerosols, *J. Geophys. Res.*, *110*, D18206, doi:10.1029/2004JD005674.

Lohmann, U., and C. Leck (2005), Importance of submicron surface-active organic aerosols for pristine Arctic clouds, *Tellus*, *57B*, 261–268.

Luo, C., N. Mahowald, and J. D. Corral (2003), Sensitivity study of meteorological parameters on mineral aerosol mobilization, transport and distribution, *J. Geophys. Res.*, *108*(D15), 4447, doi:10.1029/2003JD003483.

Mahowald, N. M., and C. Luo (2003), A less dusty future?, *Geophys. Res. Lett.*, *30*(17), 1903, doi:10.1029/2003GL017880.

Mahowald, N. M., J.-F. Lamarque, X. X. Tie, and E. Wolff (2006), Sea-salt aerosol response to climate change: Last Glacial Maximum, preindustrial,

and doubled carbon dioxide climates, *J. Geophys. Res.*, *111*, D05303, doi:10.1029/2005JD006459.

Mallet, M., J. C. Roger, S. Despiau, J. P. Putaud, and O. Dubovik (2004), A study of the mixing state of black carbon in urban zone, *J. Geophys. Res.*, *109*, D04202, doi:10.1029/2003JD003940.

Martins, J. V., P. V. Hobbs, R. E. Weiss, and P. Artaxo (1998), Sphericity and morphology of smoke particles from biomass burning in Brazil, *J. Geophys. Res.*, *103*(D24), 32,051–32,057.

Mayer, M., R. Hyman, J. Harnisch, and J. Reilly (2000), Emissions inventories and time trends for greenhouse gases and other pollutants, *Tech. Note 1*, 49 pp., MIT Joint Program on the Science and Policy of Global Change, Cambridge, Mass.

Mikhailov, E. F., S. S. Vlasenko, I. A. Podgorny, V. Ramanathan, and C. E. Corrigan (2006), Optical properties of soot–water drop agglomerates: An experimental study, *J. Geophys. Res.*, *111*, D07209, doi:10.1029/2005JD006389.

Minikin, A., A. Petzold, J. Ström, R. Krejci, M. Seifert, P. van Velthoven, H. Schlager, and U. Schumann (2003), Aircraft observations of the upper tropospheric fine particle aerosol in the Northern and Southern Hemispheres at midlatitudes, *Geophys. Res. Lett.*, *30*(10), 1503, doi:10.1029/2002GL016458.

Myhre, G., F. Stordal, K. Restad, and I. Isaksen (1998), Estimates of the direct radiative forcing due to sulfate and soot aerosols, *Tellus, Ser. B, 50*, 463–477.

Naoe, H., and K. Okada (2001), Mixing properties of submicrometer aerosol particles in the urban atmosphere - with regard to soot particles, *Atmos. Environ.*, *35*, 5765–5772.

Nenes, A., and J. H. Seinfeld (2003), Parameterization of cloud droplet formation in global climate models, *J. Geophys. Res.*, *108*(D14), 4415, doi:10.1029/2002JD002911.

Okada, K., M. Ikegami, Y. Zaizen, Y. Makino, J. B. Jensen, and J. L. Gras (2001), The mixture state of individual aerosol particles in the 1997 Indonesian haze episode, *J. Aerosol Sci.*, *32*, 1269–1279.

Okada, K., M. Ikegami, Y. Zaizen, Y. Tsutsumi, Y. Makino, J. B. Jensen, and J. L. Gras (2005), Soot particles in the free troposphere over Australia, *Atmos. Environ.*, *39*, 5079–5089.

Palmer, K. F., and D. Williams (1975), Optical constants of sulfuric acid; application to the clouds of Venus?, *Appl. Opt.*, *14*, 208–219.

Penner, J. E., et al. (2001), Aerosols and radiative forcing, in *Intergovernmental Panel on Climate Change, Report to IPCC From the Scientific Assessment Working Group (WGI)*, pp. 289–349, Cambridge Univ. Press, New York.

Petters, M. D., and S. M. Kreidenweis (2007), A single parameter representation of hygroscopic growth and cloud condensation nucleus activity, *Atmos. Chem. Phys. Discuss.*, *7*, 1961–1971.

Pósfai, M., R. Simonics, J. Li, P. V. Hobbs, and P. R. Buseck (2003), Individual aerosol particles from biomass burning in southern Africa: 1. Compositions and size distributions of carbonaceous particles, *J. Geophys. Res.*, *108*(D13), 8483, doi:10.1029/2002JD002291.

Pruppacher, H. R., and J. D. Klett (1997), *Microphysics of Cloud and Precipitation*, 954 pp., Springer, New York.

Ramanathan, V., P. J. Crutzen, J. T. Kiehl, and D. Rosenfeld (2001a), Aerosol, climate, and the hydrological cycle, *Science*, *294*, 2119–2124.

Ramanathan, V., et al. (2001b), Indian Ocean Experiment: An integrated analysis of the climate forcing and effects of the great Indo-Asian haze, *J. Geophys. Res.*, *106*(D22), 28,371–28,398.

Ramanathan, V., C. Chung, D. Kim, T. Bettge, L. Buja, J. T. Kiehl, W. M. Washington, Q. Fu, D. R. Sikka, and M. Wild (2005), Atmospheric brown clouds: Impacts on South Asian climate and hydrological cycle, *Proc. Natl. Acad. Sci. U.S.A.*, *102*, 5326–5333.

Ramanathan, V. C., M. V. Ramana, G. Roberts, D. Kim, D. Corrigan, C. Chul, and D. Winker (2007), Warming trends in Asia amplified by brown cloud solar absorption, *Nature*, *448*, 575–579, doi:10.1038/nature06019.

Ramaswamy, V., et al. (2001), Chapter 6, in *Climate Change 2001: The Scientific Basis. Contribution of Working Group 1 to the Third Assessment Report of the Intergovernmental Panel on Climate Change*, edited by J. T. Houghton et al., pp. 349–416, Cambridge Univ. Press, Cambridge.

Randles, C. A., L. M. Russell, and V. Ramaswamy (2004), Hygroscopic and optical properties of organic sea salt aerosol and consequences for climate forcing, *Geophys. Res. Lett.*, *31*, L16108, doi:10.1029/2004GL020628.

Rasch, P. J., M. C. Barth, J. T. Kiehl, S. E. Schwartz, and C. M. Benkovitz (2000), A description of the global sulfur cycle and its controlling processes in the National Center for Atmospheric Research Community Climate Model, Version 3, *J. Geophys. Res.*, *105*(D1), 1367–1386.

Riemer, N., H. Vogel, and B. Vogel (2004), Soot aging time scales in polluted regions during day and night, *Atmos. Chem. Phys.*, *4*, 1885–1893.

Russell, L. M., S. F. Maria, and S. C. B. Myneni (2002), Mapping organic coatings on atmospheric particles, *Geophys. Res. Lett.*, *29*(16), 1779, doi:10.1029/2002GL014874.

Schulz, M., et al. (2006), Radiative forcing by aerosols as derived from the AeroCom present-day and pre-industrial simulations, *Atmos. Chem. Phys. Discuss.*, *6*, 5095–5136.

Schwartz, S. E. (1996), The whitehouse effect-shortwave radiative forcing of climate by anthropogenic aerosols: An overview, *J. Aerosol Sci.*, *27*, 359–382.

Schwartz, S. E. (2004), Uncertainty requirements in radiative forcing of climate change, *J. Air Waste Manage. Assoc.*, *54*, 1351–1359.

Schwarz, J. P., et al. (2008), Coatings and their enhancement of black carbon light absorption in the tropical atmosphere, *J. Geophys. Res.*, *113*, D03203, doi:10.1029/2007JD009042.

Seinfeld, J. H., and S. N. Pandis (1998), *Atmospheric Chemistry and Physics: From Air Pollution to Climate Change*, John Wiley, Hoboken, N. J.

Stier, P., et al. (2005), The aerosol–climate model ECHAM5-HAM, *Atmos. Chem. Phys.*, *5*, 1125–1156.

Stier, P., J. H. Seinfeld, S. Kinne, J. Feichter, and O. Boucher (2006), Impact of nonabsorbing anthropogenic aerosols on clear-sky atmospheric absorption, *J. Geophys. Res.*, *111*, D18201, doi:10.1029/2006JD007147.

Stier, P., J. H. Seinfeld, S. Kinne, and O. Boucher (2007), Aerosol absorption and radiative forcing, *Atmos. Chem. Phys. Discus.*, *7*, 7171–7233.

Takemura, T., T. Nozawa, S. Emori, T. Y. Nakajima, and T. Nakajima (2005), Simulation of climate response to aerosol direct and indirect effects with aerosol transport-radiation model, *J. Geophys. Res.*, *110*, D02202, doi:10.1029/2004JD005029.

Texter, C., et al. (2006), Analysis and qualification of the diversities of aerosol life cycles within AeroCom, *Atmos. Chem. Phys.*, *6*, 1777–1813.

Toon, O. B., and T. P. Ackerman (1981), Algorithms for the calculation of scattering by stratified spheres, *Appl. Opt.*, *20*, 3657–3660.

Vehkamäki, H., M. Kulmala, I. Napari, K. E. J. Lehtinen, C. Timmreck, M. Noppel, and A. Laaksonen (2002), An improved parameterization for sulfuric acid–water nucleation rates for tropospheric and stratospheric conditions, *J. Geophys. Res.*, *107*(D22), 4622, doi:10.1029/2002JD002184.

Vignati, E., J. Wilson, and P. Stier (2004), M7: An efficient size-resolved aerosol microphysics module for large-scale aerosol transport models, *J. Geophys. Res.*, *109*, D22202, doi:10.1029/2003JD004485.

Wang, C. (2004), A modeling study on the climate impacts of black carbon aerosols, *J. Geophys. Res.*, *109*, D03106, doi:10.1029/2003JD004084.

Wang, C. (2005), A modeling study of the response of tropical deep convection to the increase of cloud condensation nuclei concentration: 1. Dynamics and microphysics, *J. Geophys. Res.*, *110*, D21211, doi:10.1029/2004JD005720.

Wilcox, E. M., and V. Ramanathan (2004), The impact of observed precipitation upon the transport of aerosols from south Asia, *Tellus*, *56B*, 435–450.

Wilson, J., C. Cuvelier, and F. Raes (2001), A modeling study of global mixed aerosol fields, *J. Geophys. Res.*, *106*(D24), 34,081–34,108.

World Climate Program (1986), A preliminary cloudless standard atmosphere for radiation computation, *Report No. WCP-112, WMO/TD-No. 24*, World Meteorolgical Organisation, Geneva.

Yu, H., et al. (2006), A review of measurement-based assessments of the aerosol direct radiative effect and forcing, *Atmos. Chem. Phys.*, *6*, 613–666.

Yum, S. S., J. G. Hudson, K. Y. Song, and B.-C. Choi (2005), Springtime cloud condensation nuclei concentrations on the west coast of Korea, *Geophys. Res. Lett.*, *32*, L09803, doi:10.1029/2005GL022641.

Zhang, D., J. Zang, G. Shi, Y. Iwasaka, A. Matsuki, and D. Trochkine (2003), Mixture state of individual Asian particles at a coastal site of Qingdao, China, *Atmos. Environ.*, *37*, 3895–3901.

————————————

M. C. Barth and P. J. Rasch, National Center for Atmospheric Research, P.O. Box 3000, Boulder, CO 80307, USA.

A. M. L. Ekman, Department of Meteorology, Stockholm University, SE-106 91, Stockholm, Sweden.

D. Kim and C. Wang, Department of Earth, Atmosphere and Planetary Science, Massachusetts Institute of Technology, MIT (Building 54-1726), 77 Massachusetts Avenue, Cambridge, MA 02139, USA. (dckim@mit.edu)